

A ternary system exploiting the full solar spectrum to generate renewable hydrogen from a waste biomass feedstock

Qiyuan Li ^{a,#}, Lixue Jiang ^{a,#}, Gan Huang ^{b,c,#}, Da-Wei Wang ^a, Jack Shepherd ^a, Rahman Daiyan ^a,
Christos N. Markides ^b, Robert A. Taylor ^{d,*}, Jason Scott ^{a,*}

^a School of Chemical Engineering, The University of New South Wales (UNSW), Kensington,
New South Wales 2052, Australia

^b Clean Energy Processes (CEP) Laboratory, Department of Chemical Engineering, Imperial College London, UK

^c Institute of Microstructure Technology, Karlsruhe Institute of Technology, Karlsruhe, Germany

^d School of Mechanical and Manufacturing Engineering, The University of New South Wales (UNSW), Kensington,
New South Wales 2052, Australia

Supplementary Information

Contributed equally to the research outcomes

* Corresponding authors: Robert A. Taylor, robert.taylor@unsw.edu.au; Jason Scott, jason.scott@unsw.edu.au

S1. Characteristics of feed wastewater and product water

The sugar-sweetened beverage industry, especially carbonated soft drinks and fruit juices (~100 g/L of sugar content) production,¹ generate a large amount of sugar containing wastewaters (~0.5 L of wastewater for every litre of the beverage produced).² They are generated from cleaning and washing processes as well as discarded product (2–5% of beverages produced) during the bottling process as a result of poor quality (e.g., a lack of gas content).¹ They exhibit high chemical oxygen demand (COD) levels of 1.6-15 g/L due to their sugar content being between 1–8 g/L, as summarized in Table S1. In this work, a mixture of sugar-sweetened drinks (3% Coca-Cola, 3.5% apple juice, 3.5% lemonade and 90% water) to simulate typical contaminant levels in beverage and sugar industry effluents.¹

Table S1. Characteristics of feed wastewater and the water produced at various stages during treatment by the waste biomass concentrator (WBC). Numbers highlighted in yellow correspond to the stream indicated in Figure 2(a).

Characteristics ^a	Levels of contamination reported for beverage and sugar industry wastewater ^a	UF + Activated charcoal		RO (Feed is the permeate from UF process)		
		Feedstock (simulated wastewater)	Permeate	Concentrated Feed	Permeate (RO 1)	Permeate (RO 2)
		1	2	3	4	5
pH	3.4-12 ³⁻⁵	3.38	2.98	1.70	4.60	4.80
Conductivity (µS/cm)	266 – 2,230 ^{3, 4, 6}	357	538	766	52	16
Colour (Absorbance _{466-610nm})	Dark yellow, dark grey or black ⁶	0.1-0.5	0.001-0.004	0.11-0.22	0.007-0.01	0.001-0.005
Sugar (mg/L)	1,350-7,972 ⁴	1° Brix (10 g/L)	1° Brix (10 g/L)	3.5° Brix (~35 g/L)	0.2° Brix (~2 g/L)	0° Brix
COD	1,616- 15,000 ^{3-5, 7}	12,000	11,400	42,200	311	15
TOC	1,987-5,200 ^{3, 8}	4,007	3,783	13,432	204	6.8
TIC (CO ₃ and HCO ₃)	168-662 ^{3, 4}	5.7	0.03	3.7	3.2	1.0
Total nitrogen	22-49 ⁵	12.7	15.2	38.6	1.0	0.8
Total phosphorus	4-130 ⁵	6.7	49.5	162	5.5	0.1
Magnesium	0-268 ⁶	3.1	2.8	9.5	0.1	N/A
Calcium	13-361 ^{4, 6}	2.2	1.8	8.9	0.3	0.04
Sodium	83-183 ⁴	4.0	6.2	26.6	0.8	0.2
Potassium	70-113 ⁹	47.8	46.6	156.8	3.0	0.4
Sulphate	5.0-419 ^{4, 6, 9}	5.0	5.8	20.2	1.1	N/A
Phosphate	1.2-40 ^{4, 9}	15.7	152	460	15.3	N/A
Chloride	20-45 ⁴	4.3	5.7	11.0	5.5	2.8

Note a: TSS, total suspended solids; TDS, total dissolved solids; COD, chemical oxygen demand; TOC, total organic carbon; TIC, total inorganic carbon. Except colour, pH, and conductivity all values are in mg/L.

Values for the individual constituents in the feed wastewater and the water produced at various stages of treatment by the waste biomass concentrator (WBC) are provided in Table S1 with a photo of the respective water samples in Figure S1. These were measured using a range of devices/methods. The pH and conductivity were measured by a benchtop pH/EC meter (HI5521-02 from Hanna instruments, Australia). The colour was indicated by measuring the absorbance of 4 wavelengths of light (466 nm, 525 nm, 575 nm, and 610 nm) using a multiparameter photometer (HI83399 from Hanna instruments, Australia). The sugar content (% Brix) was determined by measuring refractive index/Brix using a portable refractometer (HI96801 from Hanna instruments, Australia). The COD of the samples was determined using the closed dichromate-reflux colorimetric method. The samples were added to the reagent vials (Reagent kit HI93754C-25 from Hanna instruments), digested under closed reflux conditions using a COD digester (HI839800-02, from Hanna instruments) and measured by benchtop photometer (HI83314 from Hanna instruments). P, N, Mg, Ca, Na, and K were analysed by Inductively Coupled Plasma-Optical Emission Spectroscopy (ICP-OES) (Optima7000 and Avio from PerkinElmer, USA) and Inductively Coupled Plasma Mass Spectrometry (ICP-MS) (Nexion5000 from PerkinElmer, USA). SO_4^{2-} , PO_4^{3-} and Cl^- were measured by anion chromatography systems (Dionex ion chromatograph from ThermoFisher, USA, and a Metrohm ion chromatograph, Switzerland). TOC, TIC and DOC were measured by a TOC analyser (multi N/C 3100 from Analytic Jena, Germany).

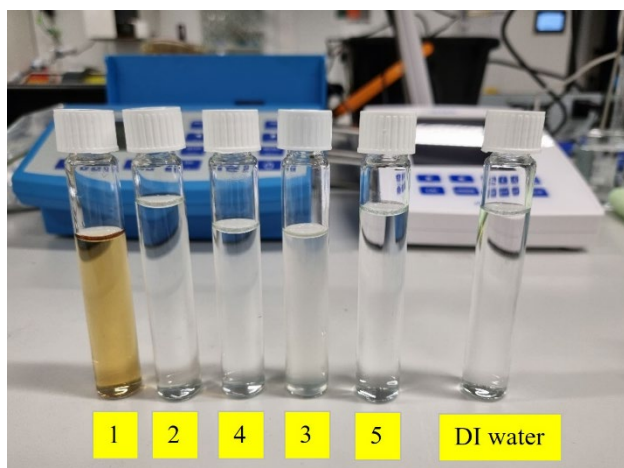


Figure S1. Image showing the colour of the feed wastewater and the water produced at various stages during treatment by the waste biomass concentrator (WBC). Numbers highlighted in yellow correspond to the stream indicated in Figure 2(a).

S2. Material and experimental methods

PV-driven waste biomass concentrator (WBC): Figure S2(a-b) provide explosive views of the ceramic ultrafiltration (UF) membrane module and reverse osmosis (RO) membrane module. One UF module comprises of 9 membranes, giving a total of membrane area of 0.045 m² per module, while the RO element (TW30HP-4611, DuPont Filmtec, USA) has 2.2 m² membrane area. All membranes (UF or RO) were sealed with rubber seals and Nitrile o-rings (3.53 mm cross-section diameter), held in place using custom-made end caps (PVC material, manufactured at UNSW workshop), M6 threaded rods and tightening nuts (Bunnings, Australia).

As shown in Figure S2(c), the water treatment testing rig comprises a PV power source, membrane modules (UF or RO), pump and piping instruments (e.g., tanks, feed inlet and outlet pressure gauges, pressure relief valve, purchased from Swagelok Australia). The DC feed pump (Model 1322-12, Dankoff SlowPump, USA) is capable of achieve a maximum pressure of 17 bar at a flow rate of 0.7 L/min, while the pump controller (DC-DC buck-type converter WZ5012L, purchased from Hong Kong

Feng Tai Co., LTD) regulates the voltage from the battery to run the DC pump. The PV power system was purchased from Renogy Australia. It consists of a 100 Watt solar panel (cell efficiency 21%), a Rover 20A maximum power point tracking (MPPT) charge controller, and a 12 V 50 Ah lithium iron phosphate battery. The feed operating pressure was set in the range of 5–10 bars by adjusting the valve and pump controller. The transmembrane water flux [$\text{L}\cdot\text{m}^{-2}\cdot\text{h}^{-1}$] can be calculated from the membrane permeability and transmembrane pressure.

$$J = K_m \cdot (P_f - P_p - \pi) \quad (\text{S1})$$

where K_m represents the pure water permeability of the membrane, with an average value of $3.4 [\text{L}\cdot\text{m}^{-2}\cdot\text{h}^{-1}\cdot\text{bar}^{-1}]$ for the RO membrane module, determined from the experiments by circulating deionized water as feed solution at pressure from 2 to 10 bars. P_f , P_p and π are the feed, permeate and osmosis pressures. The osmotic pressure of sugar solution can be expressed as:

$$\pi = C \cdot R \cdot T \quad (\text{S2})$$

where C is the molar concentration [$\text{mol}\cdot\text{L}^{-1}$] of neat sucrose or fructose solution, R is the ideal gas constant ($0.0821 \text{ L atm}\cdot\text{mol}^{-1}\cdot\text{K}^{-1}$), and T is the temperature in Kelvin (298 K).

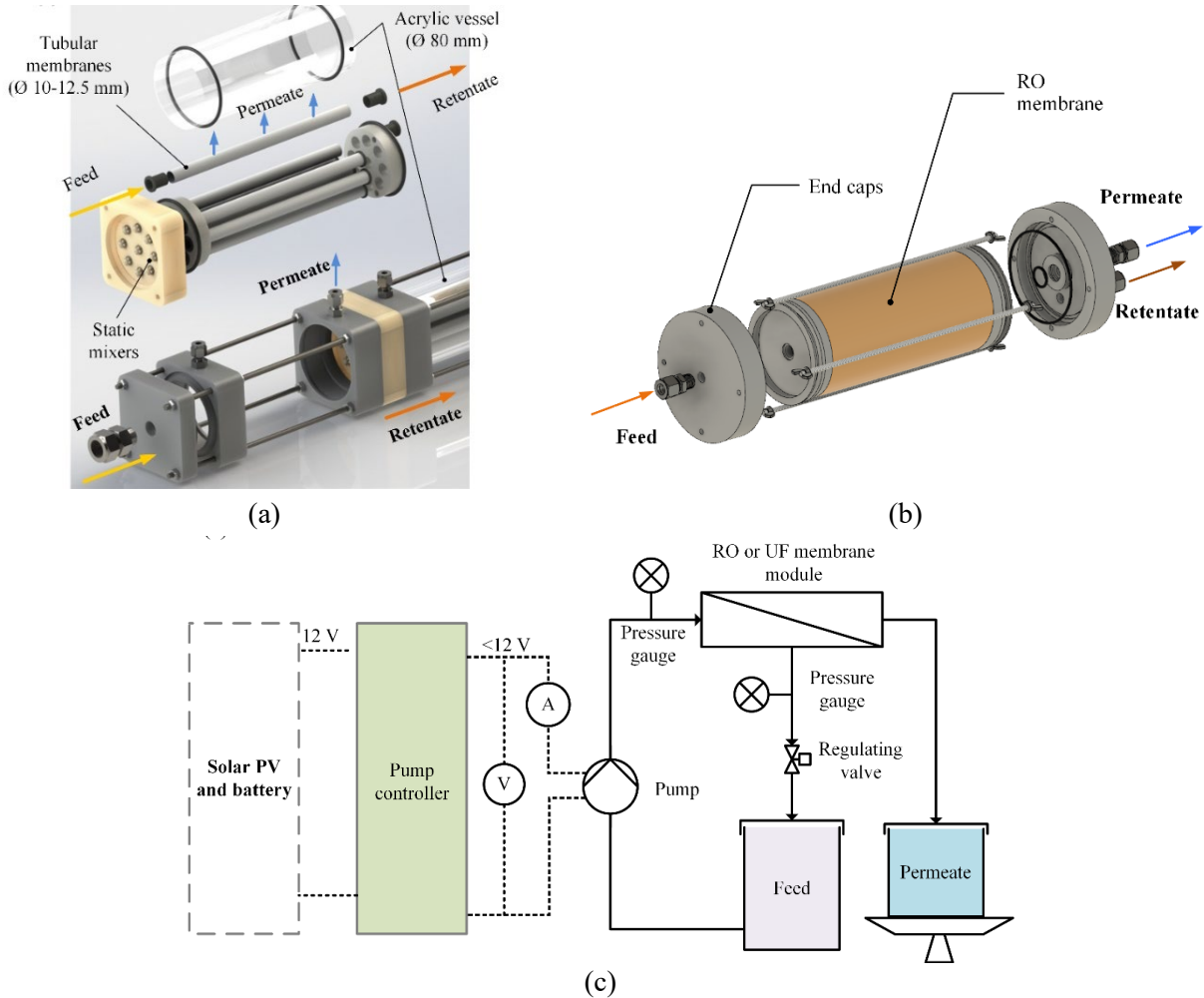


Figure S2. Module/system and PV-battery powered system for the WBC: (a) ceramic ultrafiltration module (9 pieces of Filtanium Ceramic Membrane, 100 KDa, 10 mm OD x 250 mm length per tube, 0.045 m^2 area/module); (b) explosive view of the RO module (Filmtec TW30HP-4611, Polyamide Thin-Film Composite, 2.2 m^2 area/module); (c) diagram of filtration testing system.

PV-thermal biomass preconditioning reactor (BPR): Figure S3(a) gives a 3D view of a concept PV-thermal BPR module design with a future flexible semi-reflective solar cell. The module unit consists of a flexible semi-reflective PV wing, a solar tube biomass reactor, a compound parabolic

concentrator (CPC) and a Geneva device to rotate/lock the wings.¹⁰ Details on the CPC (3D printed, building material was VisiJet CR-CL 200, ProJet® MJP 5600 printer) and the solar tube (borosilicate glass, Apricus Australia) were reported in our previous work.¹⁰

Semi-reflective and flexible solar cells based on emerging thin film technologies (e.g., Cu(In,Ga)Se₂ (CIGS) and CdTe) are key development directions for future improvement of the BPR, as they can be beneficial for both production (using a roll-to-roll approach) and application (easy installation on solar concentrators). However, conventional CdTe-based cells are fabricated in a ‘superstrate structure’ with the layers being deposited onto the front glass (where light enters through the glass substrate into the solar cell), limiting the choice of substrates to transparent materials. To allow the use of flexible and reflective metal foil substrates, the conventional CdTe device structure needs to be inverted (starting with growing an electrical back contact layer on the metal foil substrate). However, it imposes severe restrictions on device processing and consequently limits the electronic quality of the CdTe layer.¹¹⁻¹³ In the case of CIGS, the reactivity of the absorber layer deposition process leads to best results in the substrate configuration in combination with molybdenum as a back contact.¹² To date, photovoltaic efficiency values greater than 18% have been demonstrated for CIGS solar (mini)modules fabricated on non-glass flexible substrates¹⁴, while various efforts to grow CdTe solar cells on metal foil have resulted in lower efficiencies (<13.6%)¹¹. Thus, a flexible semi-reflective CIGS based solar cell is proposed for future systems, with a schematic of CIGS solar cell structure shown in Figure S3 (b). The thickness and materials of each layer in the thin film CIGS solar cell were designed based on recently reported flexible thin film solar cell studies (as summarized in Table S2).¹⁴⁻¹⁷ As a more common structure, the CIGS film (2 μm thick) can be grown on Mo (0.5-1 μm thick)-coated flexible substrates (e.g., stainless steel or flexible ceramic sheets, 150-200 μm thickness), so the Mo metal film (0.5-1 μm thick) acts as an electrical back contact and an optical reflector.¹⁸ Alternatively, the CIGS absorbers can be deposited on a ~150 μm flexible Mo foil. The metal foil can be used as both the substrate and back contact which reduces the manufacturing steps of this type of solar cell (eliminating the need for a sputtered Mo back contact).¹⁹

Table S2. Typical structure, thickness and materials for flexible CIGS solar cell ^{12, 14, 19-22}.

Material	Thickness
Transparent polymer (e.g., ETFE / PDMS foil)	25-50 μm
Epoxy glue / EVA	0.45 mm
Antireflective (AR): MgF ₂ coating	100 nm
Transparent conductive oxide (TCO) layer: aluminium-doped zinc oxide (ZnO)	300 -400 nm
TCO layer: intrinsic ZnO (i-ZnO)	50 -100 nm
Buffer layer: CdS	30-70 nm
p-type absorber layer: CIGS	2,000 nm
Electrical back contact layer: sputtered molybdenum	500-1000 nm thickness
Flexible substrates: Metallic foils (stainless steel or titanium, or molybdenum) or ceramic sheets	Stainless steel foil (thickness 75-200 μm); or Mo foil (150 μm), or 200 μm flexible ceramic sheets.

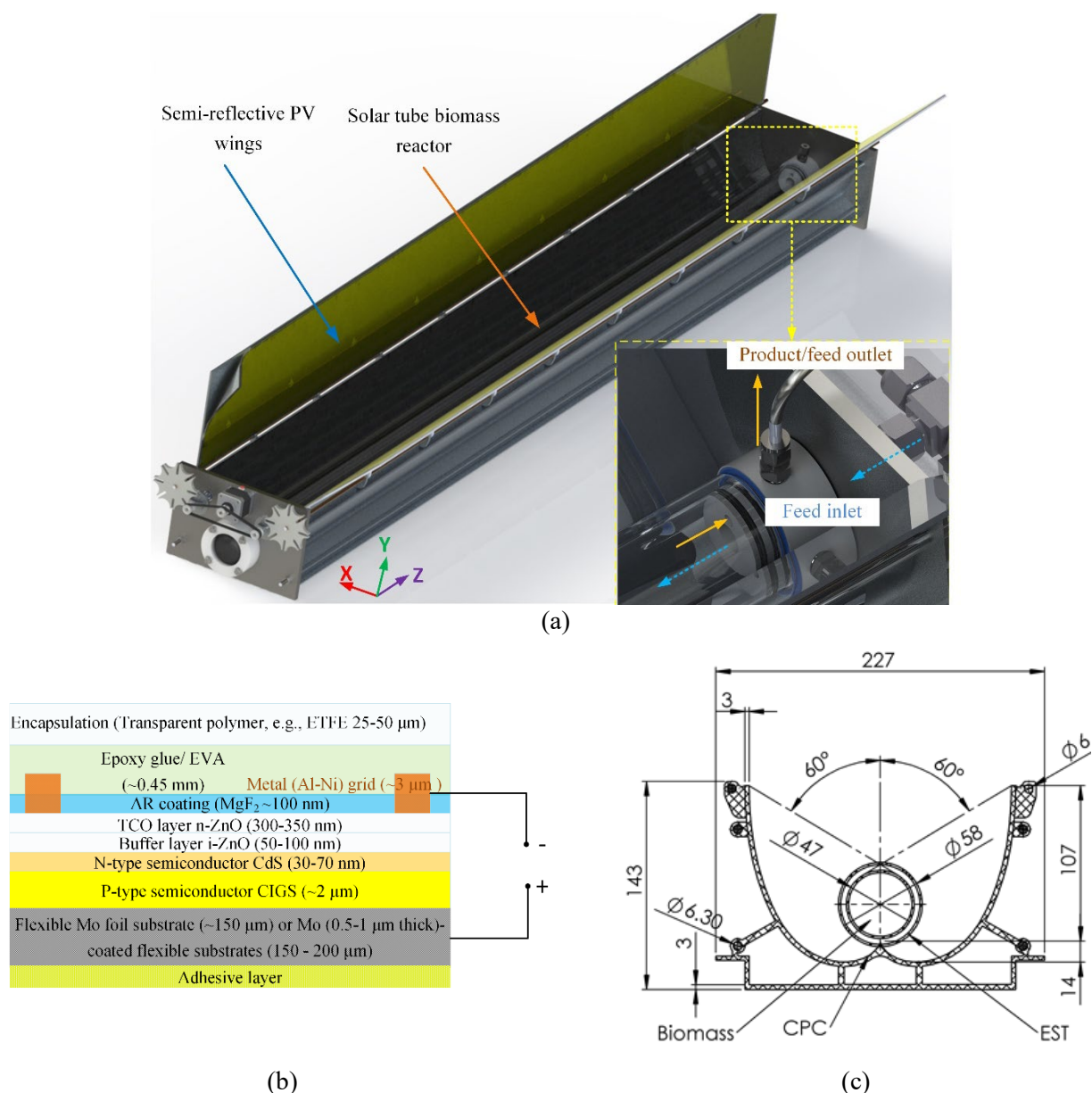


Figure S3. Module design of PV-thermal BPR: (a) the design concept with flexible semi-reflective PV wing; (b) a flexible semi-reflective solar cell design (CIGS thin film deposited on a flexible Mo foil substrate or on Mo coated flexible substrates); (c) CPC profile.

Flow electrolyser cell (FEC): As shown in Figure S4, the alkaline FEC comprises two polytetrafluoroethylene (PTFE) plates, two copper current collectors, two graphite plates with grooves, two electrodes, one anion exchange membrane (Fumasep FAA-3-PK-130), and gaskets (0.2 mm thickness EPDM). The electrode (7.9 cm \times 7.9 cm) used in this work is commercial Ni foam (purchased from MTI Corporation, purity > 99.99%, porosity \geq 95%, surface density 346 g m⁻²), which serves as both the anode for 5-HMF oxidation and the cathode for hydrogen production. Detailed information, including chemicals, preparation of NiMo electrode, and characteristics of the electrodes are reported as follows:

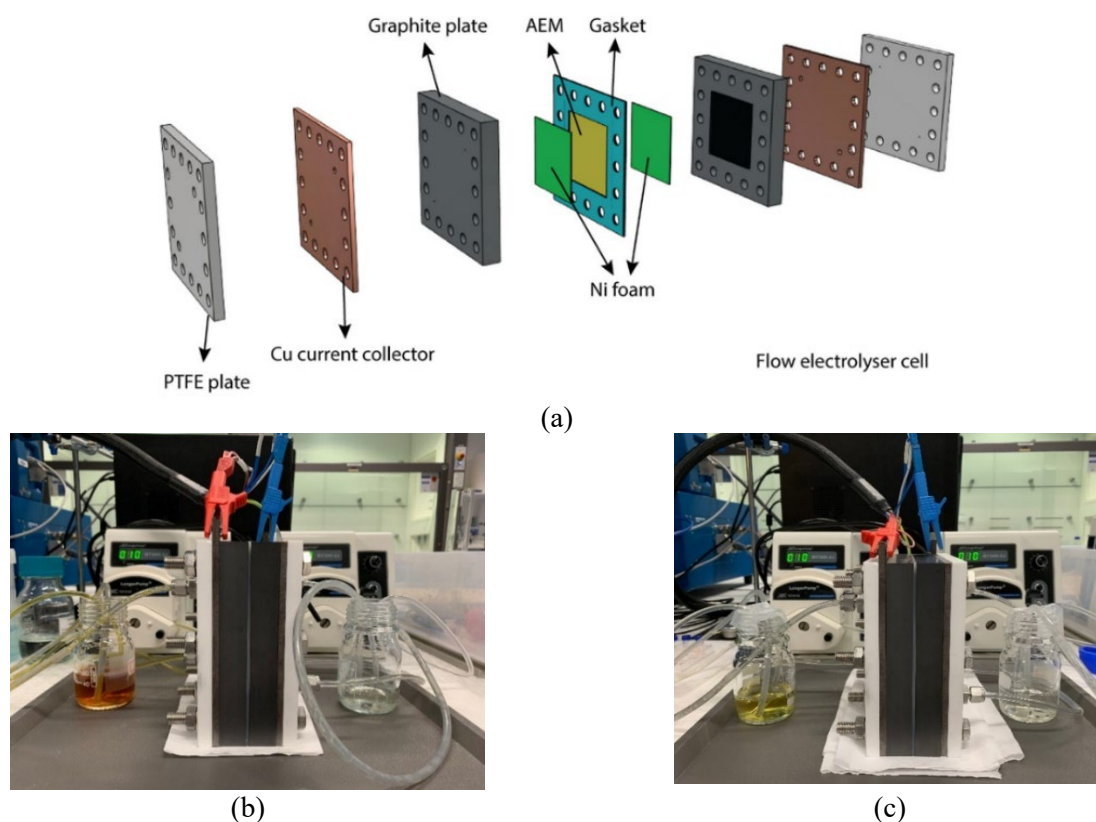


Figure S4. Flow electrolyser cell design and setup: (a) the components of the FEC used in this work. (b) FEC setup for BPR product solution electrolysis. (c) FEC setup for 5-HMF electrolysis.

Chemicals

Nickel foam (99.99% purity, MTI Corporation), nickel (II) sulfate hexahydrate ($\text{NiSO}_4 \cdot 6\text{H}_2\text{O}$, ACS reagent, $\geq 98\%$, Sigma-Aldrich), sodium molybdate dihydrate ($\text{Na}_2\text{MoO}_4 \cdot 2\text{H}_2\text{O}$, ACS reagent, $\geq 99\%$, Sigma-Aldrich), sodium citrate dihydrate ($\text{Na}_3\text{C}_6\text{H}_5\text{O}_7 \cdot 2\text{H}_2\text{O}$, $\geq 99\%$, FG, Sigma-Aldrich), potassium hydroxide (KOH, Reagent grade, 90%, flakes, Sigma-Aldrich), hydrochloric acid (HCl, 32%, RCI Premium, RCI Labscan), ethanol ($\text{C}_2\text{H}_5\text{OH}$, 100% Undenatured, Chem-supply), ammonia 30% solution (NH_4OH , Chem-supply), were used as received. Deionized (DI) water ($18.2 \text{ M}\Omega \cdot \text{cm}$ resistivity) was used for the preparation of all aqueous solutions.

Preparation of NiMo alloy on Ni foam

The NiMo alloy layer was synthesized on the surface of Ni foam in a two-electrode electrochemical cell via a modified electrodeposition method following a previously published paper (M. Gao et al.).²³ In a typical synthesis, a piece of Ni foam with a geometric area of $10.0 \times 8.0 \text{ cm}^2$ was first ultrasonically cleaned in absolute ethanol for 15 min and then in 3 M HCl aqueous solution for 15 min to remove the surface NiO_x layer. Then, the de-passivated Ni foam was rinsed with deionised water and absolute ethanol three times respectively, followed by drying at $60 \text{ }^\circ\text{C}$ in a vacuum oven for 2 h. The electrolyte was a mixture of $40 \text{ mmol L}^{-1} \text{ NiSO}_4 \cdot 6\text{H}_2\text{O}$, $40 \text{ mmol L}^{-1} \text{ Na}_2\text{MoO}_4 \cdot 2\text{H}_2\text{O}$, and $40 \text{ mmol L}^{-1} \text{ Na}_3\text{C}_6\text{H}_5\text{O}_7 \cdot 2\text{H}_2\text{O}$, and NH_4OH . In the electrodeposition process, the cleaned Ni foam was used as the working electrode and immersed in the electrolyte with an area of $8.0 \times 8.0 \text{ cm}^2$ under the solution. A graphite plate ($10.0 \text{ cm} \times 10.0 \text{ cm}$) was used as both the counter and reference electrode. The applied current density was fixed at -40 mA cm^{-2} , and the deposition time was 30 min. After deposition, the obtained NiMo alloy/Ni foam electrode was carefully withdrawn, rinsed with deionised water and absolute ethanol three times, and then dried at $60 \text{ }^\circ\text{C}$ in a vacuum oven overnight.

Preparation of NiMo alloy on carbon cloth

To conduct additional physical and electrochemical measurements (where the result may be impacted by the presence of the Ni foam) the NiMo alloy was electrochemically loaded onto a carbon cloth substrate as well. The NiMo alloy was electrodeposited on the surface of carbon cloth using the same method as above. The carbon cloth substrates were first pre-treated in a mixed nitrate acid and sulphate acid solution at 60 °C for 12 hours to generate a hydrophilic surface with oxygen-rich functional groups.²⁴

Physical characterisation

The morphologies and structures of the as-prepared NiMo alloy electrodes were characterised by scanning electron microscopy (SEM, JSM-7001F). X-ray diffraction (XRD) patterns were obtained on a Bruker D8 Advance diffractometer equipped with a graphite monochromator. A Renishaw inVia spectrometer with a 532 nm excitation laser was used to obtain the Raman spectra. X-ray photoelectron spectroscopy (XPS) was performed using a Kratos Axis ULTRA featuring a 165 mm hemispherical electron energy analyser.

Electrochemical characterisation

The electrocatalytic activities of NiMo electrodes towards the hydrogen evolution reaction (HER), oxygen evolution reaction (OER) and biomass (neat 5-HMF and BPR product stream) oxidation reaction were initially assessed in a three-electrode cell in alkalified pure water and biomass solutions. The biomass solution, comprising either 50 mM 5-HMF solution or the product stream from the BPR unit (containing ~50 mM 5-HMF), was alkalified to a pH of 14 using KOH. The NiMo alloy or Ni foam (1.0 cm × 2.0 cm with the lower 1.0 cm × 1.0 cm immersed in the electrolyte) was directly used as the working electrode, and Hg/HgO electrode and graphite rod were used as the reference electrode and counter electrode, respectively. All electrochemical measurements were conducted using a BioLogic SP-150 Potentiostat coupled with a current booster (up to 20 V and 20 A). Before recording, the potentials of the NiMo electrodes were scanned at a scan rate of 50 mV s⁻¹ until a stable cyclic voltammogram (CV) curve was recorded, and then linear sweep voltammetry (LSV) curves were recorded at a scan rate of 5 mV s⁻¹. The potentials obtained from the three-electrode cell and displayed in this work were converted to the reversible hydrogen electrode (RHE) scale using the following equation: $E_{\text{RHE}} = E_{\text{Hg/HgO}} + 0.059 \text{ pH} + 0.098 \text{ V}$. All the polarisation curves were not corrected with iR compensation and Tafel slopes were derived from the as-obtained polarisation curves. Electrochemical impedance spectroscopy (EIS) was performed across a frequency range of 100 kHz to 0.1 Hz with an amplitude of 5 mV. The potentials for EIS were set to be -0.276 V vs. RHE for HER, and 1.424 V vs. RHE for both 5-HMF and BPR products. The electrochemical surface area (ECSA) of the NiMo catalyst was estimated by measuring the electrochemical double-layer capacitance (C_{dl}) as there is a defined relationship between them: $\text{ECSA} = C_{\text{dl}} / C_s$, where C_s is the specific capacitance of the material per unit area under identical electrolyte conditions.²⁵ The CVs were reported with different rates from 10 to 100 mV s⁻¹ in the potential interval of 0.884 to 0.984 V vs. RHE. Stability tests for the NiMo electrodes for HER and OER were assessed using chronopotentiometry at a current density of 50 mA cm⁻² for more than 12 hours. In a two-electrode system, the NiMo electrode and Ni foam were used both as the anode and cathode. CV curves were scanned initially in a voltage range of 1.0-2.5 V at a scan rate of 50 mV s⁻¹ until a stable CV curve was obtained. Then LSV curves were recorded at a scan rate of 5 mV s⁻¹. The long-term durability for overall water splitting was carried out at a current density of 50 mA cm⁻² for more than 12 hours.

The anion exchange membrane (AEM) flow electrolyser cell (FEC) was assembled with Ni foam-based electrodes (NiMo/Ni foam and bare Ni foam), AEM (Fumasep FAA-3-PK-130), graphite plates with designed flow channels, copper current collectors, polytetrafluoroethylene (PTFE) end plates, and silicone gaskets. The Fumasep FAA-3-PK-130 AEM was soaked in 1 M KOH for 48 hours before use. The FEC was first scanned between 1.0 V and 2.5 V at a scan rate of 50 mV s⁻¹ until a stable CV curve was obtained. Then the LSV curves were recorded at a scan rate of 5 mV s⁻¹. The flow rate of

the electrolyte was set at 10 mL min⁻¹. The durability of hydrogen production in FEC was conducted with a chronopotentiometry technique at 50 mA cm⁻².

Additional electrodes characteristics and performance

Additional characteristics and performance are provided in Figure S5-S13, including SEM, XRD, Raman, and XPS analyses on the pristine NiMo/Ni foam electrode and the NiMo/Ni foam electrode after the HER, OER, and 5-HMF oxidation reaction.

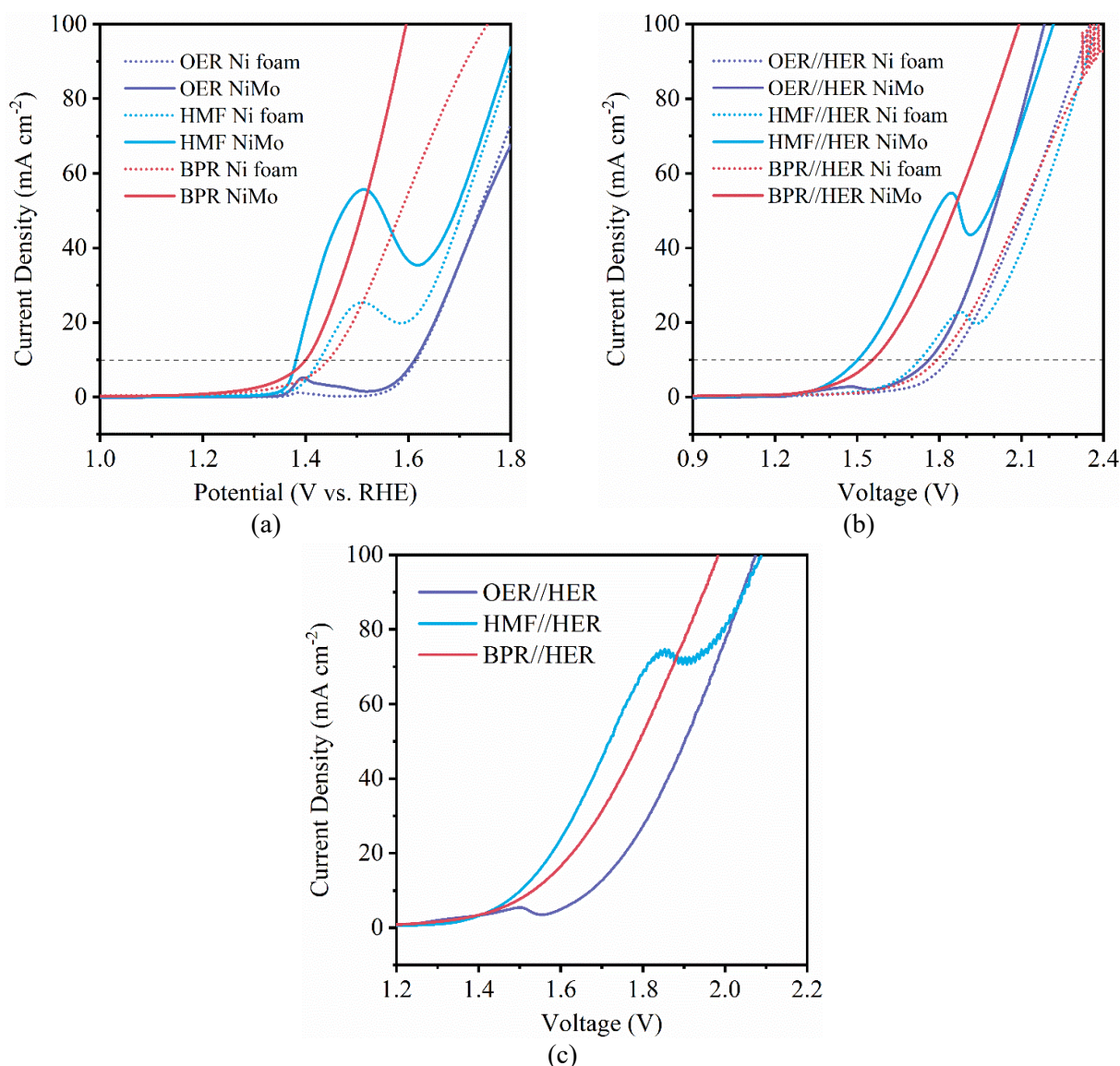


Figure S5. Electrocatalytic activity of NiMo alloy and Ni foam electrodes: (a) OER LSV curves of Ni foam and NiMo electrodes tested in alkalified pure water, 5-HMF and BPR solutions. (b) LSV curves of NiMo //NiMo vs. Ni foam//Ni foam for overall water splitting tested in alkalified pure water, 5-HMF and BPR solutions. (c) LSV curves for biomass electrolysis and water splitting using NiMo electrodes ('BPR' term denotes product stream from BPR unit mixed with 1M KOH)

Figure S5 (a) indicates that the NiMo electrode enables electro-oxidation of the alkalified 5-HMF and BPR product solutions, delivering a current density of 10 mA cm⁻² at a potential of 1.38-1.4 V. The value is slightly lower than Ni foam (1.42-1.43 V) while being significantly lower than the OER using Ni foam (1.62 V). The LSV curves in Figure S5 (b) show that the assembled NiMo//NiMo electrolysis cell can achieve a current density of 10 and 100 mA cm⁻² at a voltage of 1.52- 2 V for BPR electrolysis, 1.5-2.2 V for 5-HMF electrolysis, and 1.76-2.2 for water splitting, which outperforms the Ni foam//Ni foam arrangement in all cases.

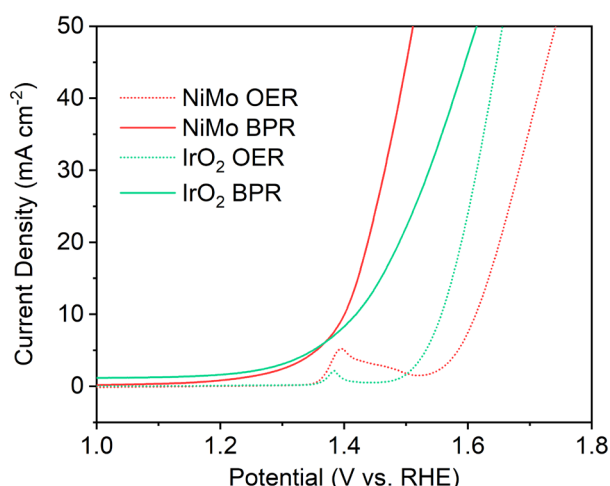


Figure S6. Activity comparison of NiMo catalyst from this work with a commercial IrO₂ catalyst. ('BPR' denotes product stream from BPR unit mixed with 1M KOH)

An IrO₂/Ni foam electrode was fabricated and tested for the OER and oxidation of the BPR solution, with the performance compared with our NiMo electrode (Figure S6). Although the IrO₂/Ni foam exhibited a higher OER activity compared to the NiMo electrode, its performance for BPR product oxidation was lower.

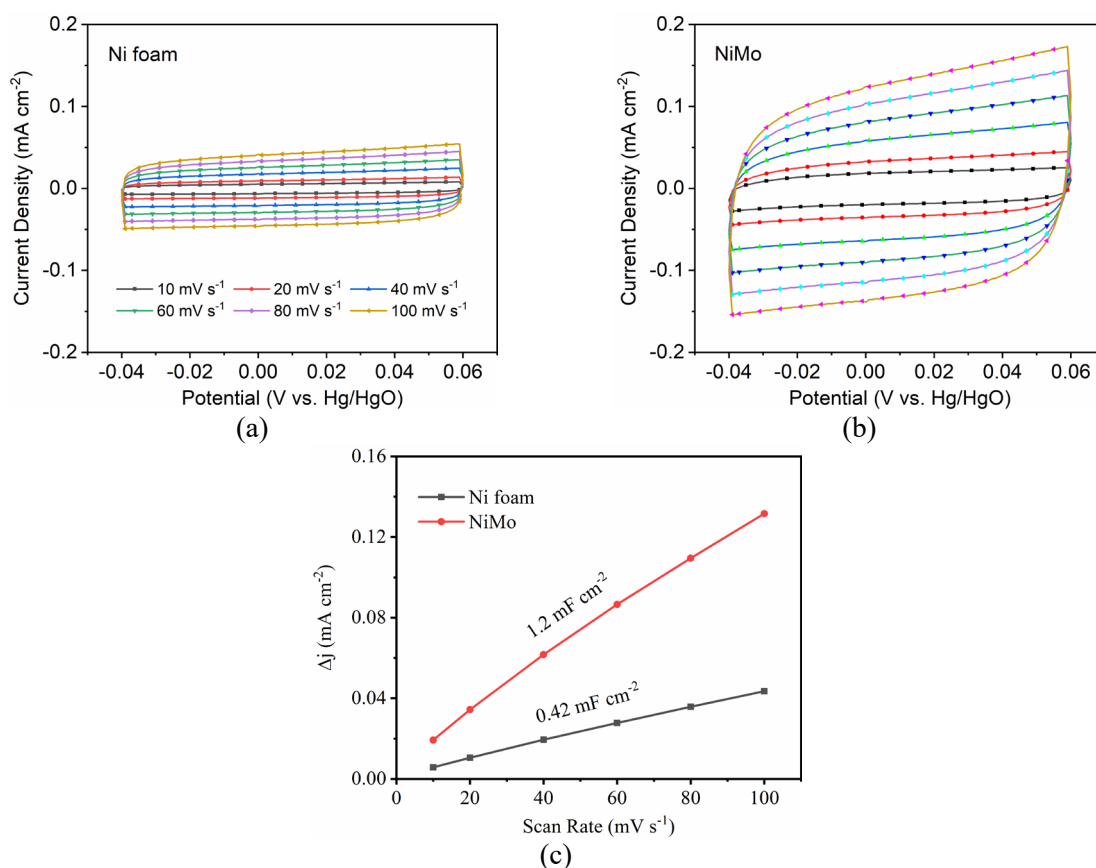


Figure S7. Capacitive current curves of (a) Ni foam and (b) NiMo electrode at different scan rates from 10 to 100 mV s⁻¹ in the potential range of 0.884 to 0.984 V vs. RHE. (c) The averaged current density differences at the potential of 0.934 V vs. RHE against the scan rates.

The electrochemical surface area (ECSA) of the NiMo electrode was estimated by measuring the electrochemical double-layer capacitance (C_{dl}) as ECSA is directly proportional to C_{dl} . The C_{dl} was determined from the slope of the averaged current density differences (Δj) against the scan rates. The

NiMo catalyst has a much higher C_{dl} (1.2 mF cm^{-2}) than that (0.42 mF cm^{-2}) of commercial Ni foam (Figure S7), indicating its high exposure of active sites.

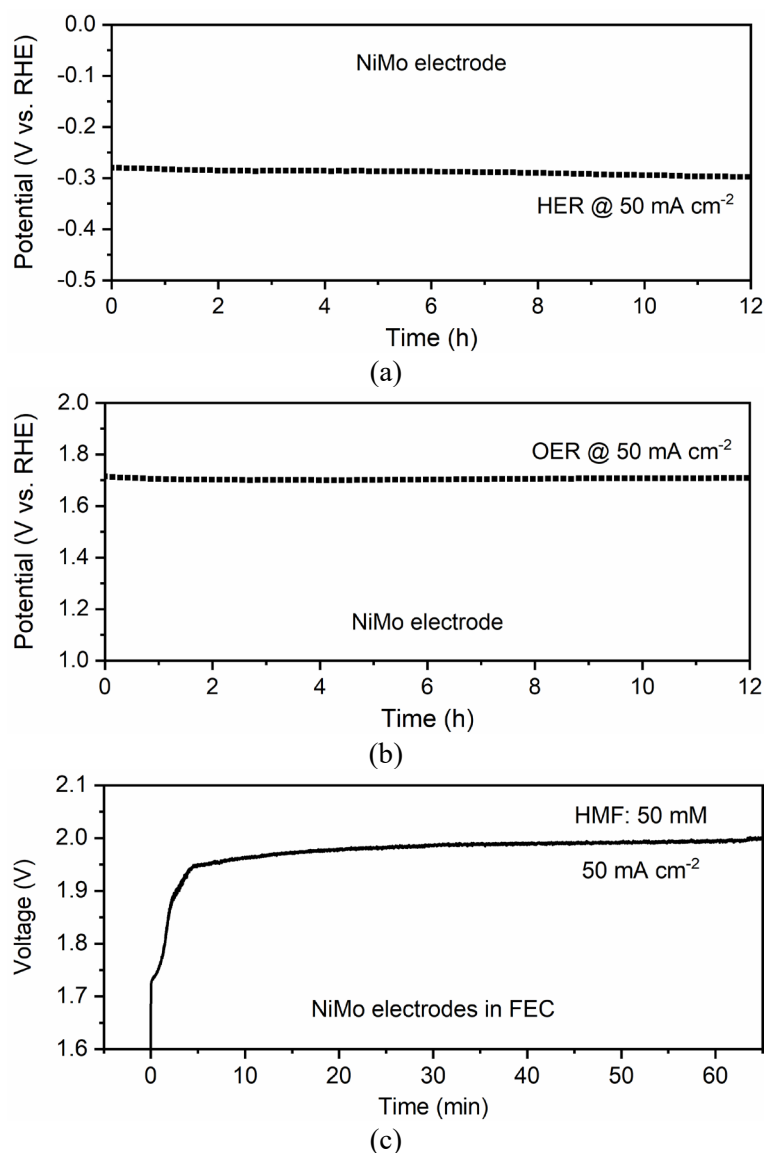


Figure S8. Chronopotentiometry tests of NiMo electrodes: (a) HER at a current density of 50 mA cm^{-2} for more than 12 hours, (b) OER at 50 mA cm^{-2} for more than 12 hours, and (c) 5-HMF oxidation and hydrogen production in the assembled FEC at 50 mA cm^{-2} for more than 60 minutes.

As shown in Figure S8, the NiMo electrodes exhibited excellent operational stability for both the HER and OER at a current density of 50 mA cm^{-2} for more than 12 hours. For 5-HMF oxidation coupled with hydrogen production in the assembled FEC, the 5-HMF molecules were consumed quickly at 50 mA cm^{-2} (3200 mA) in about five minutes, after which the OER then occurred simultaneously.

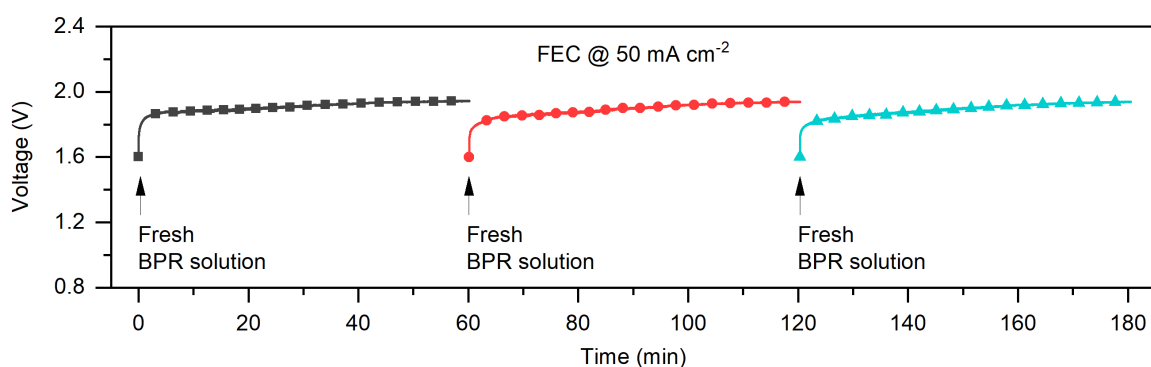


Figure S9. Durability of hydrogen production in the FEC over three consecutive experiments with each at 50 mA cm⁻² for 60 minutes.

The durability of hydrogen production in the FEC was examined by three consecutive experiments with each at 50 mA cm⁻² for 60 minutes. The reactant biomass molecules (e.g., 5-HMF) were consumed quickly and the required cell voltage increased. After replenishing the cell with fresh BPR solution, the initial cell voltage (around 1.8 V) was recovered (Figure S9).

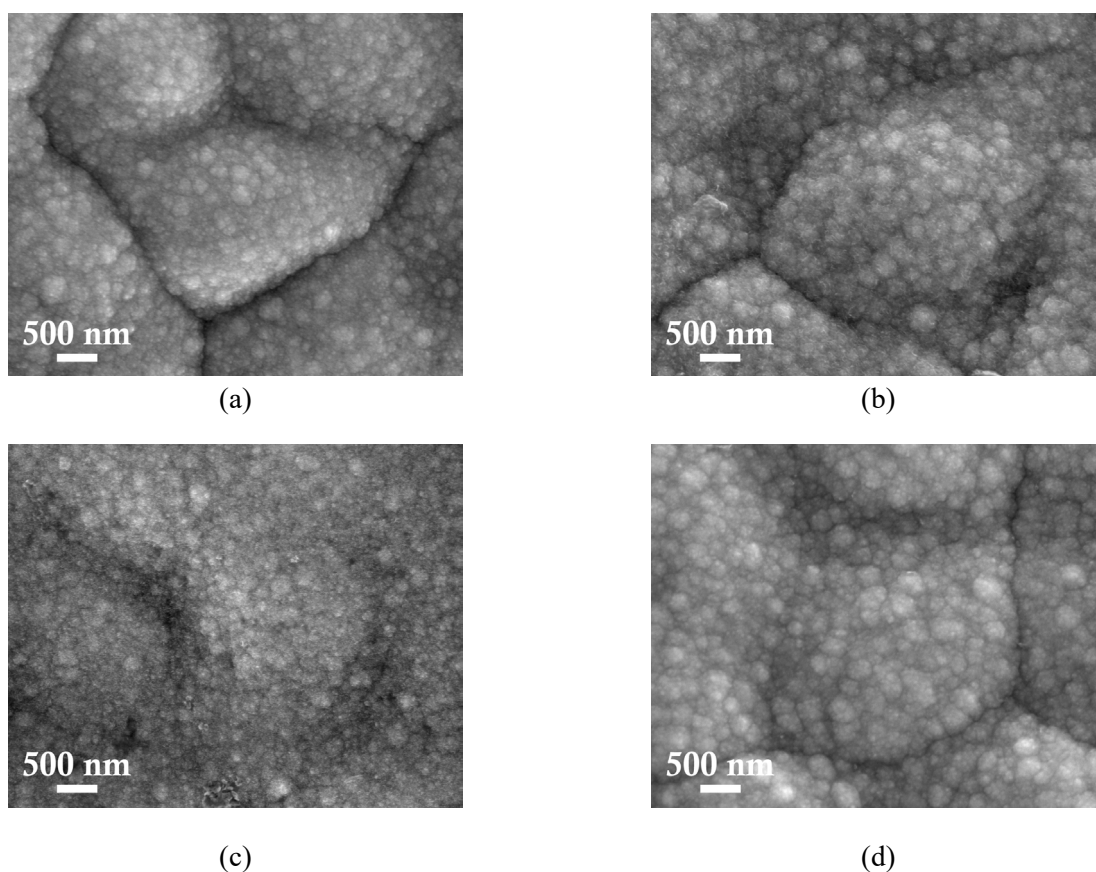


Figure S10. SEM images of (a) the pristine NiMo/Ni foam and the NiMo/Ni foam electrode after (b) HER, (c) OER, and (d) 5-HMF oxidation reaction

As shown in the SEM images (Figure S10), the morphology of the NiMo catalyst does not change significantly after the HER and 5-HMF oxidation reaction. However, after the OER, NiMo oxides/hydroxides nanoparticles appear on the surface of the NiMo alloy, which is due to structural reconstruction at higher oxidative potentials.

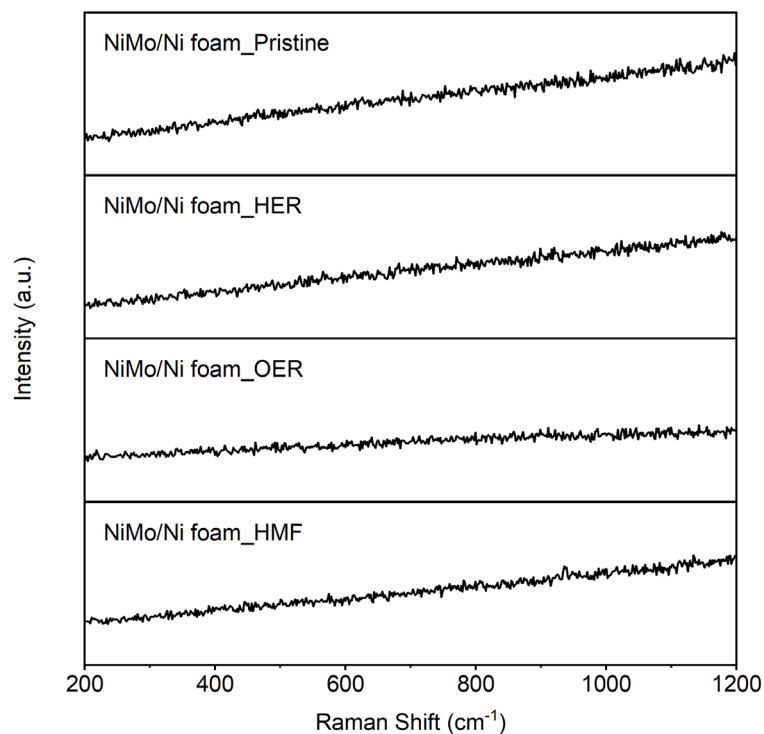
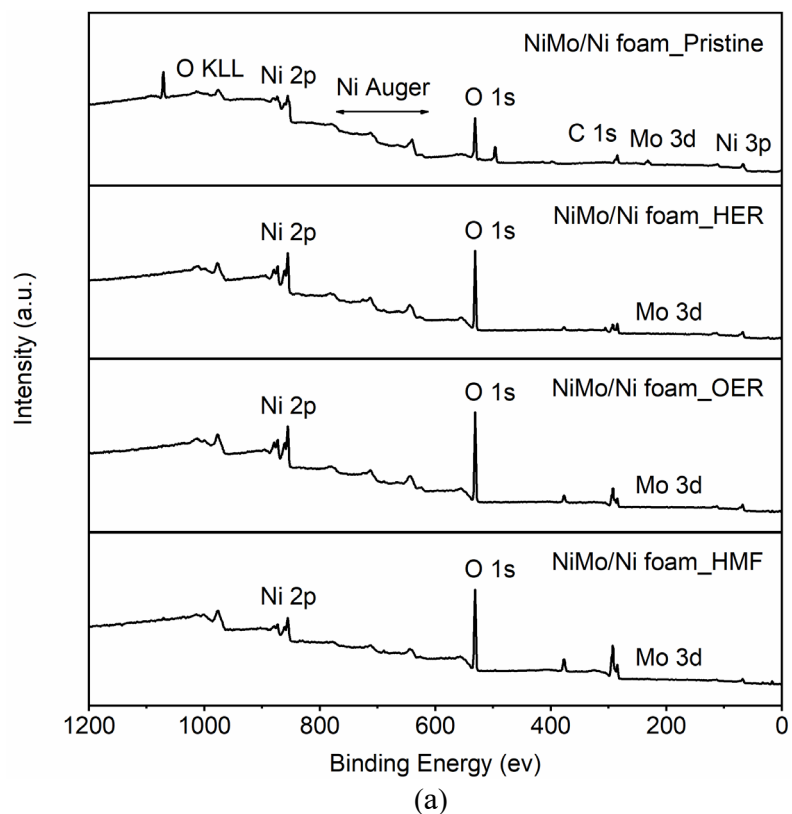
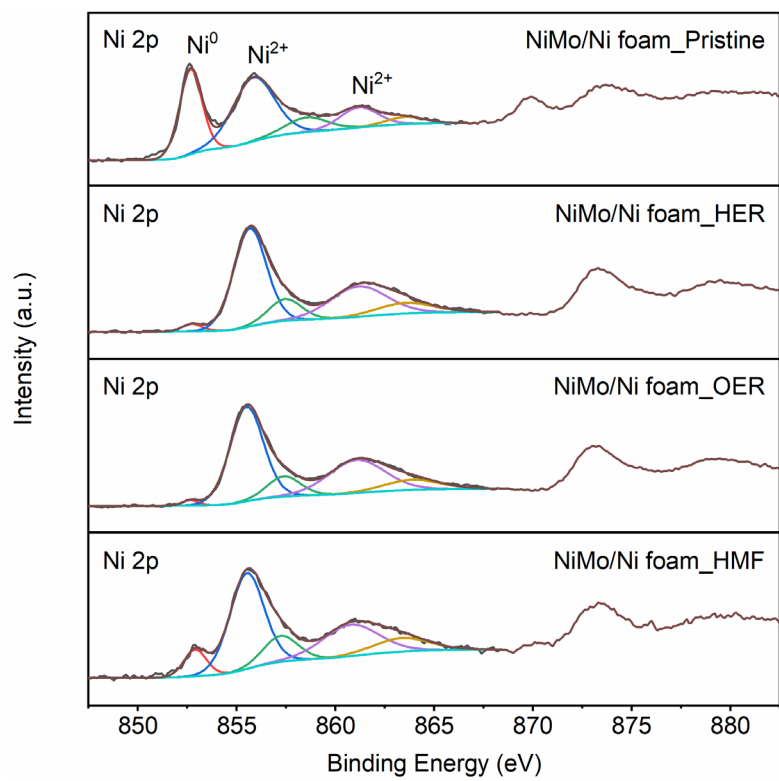


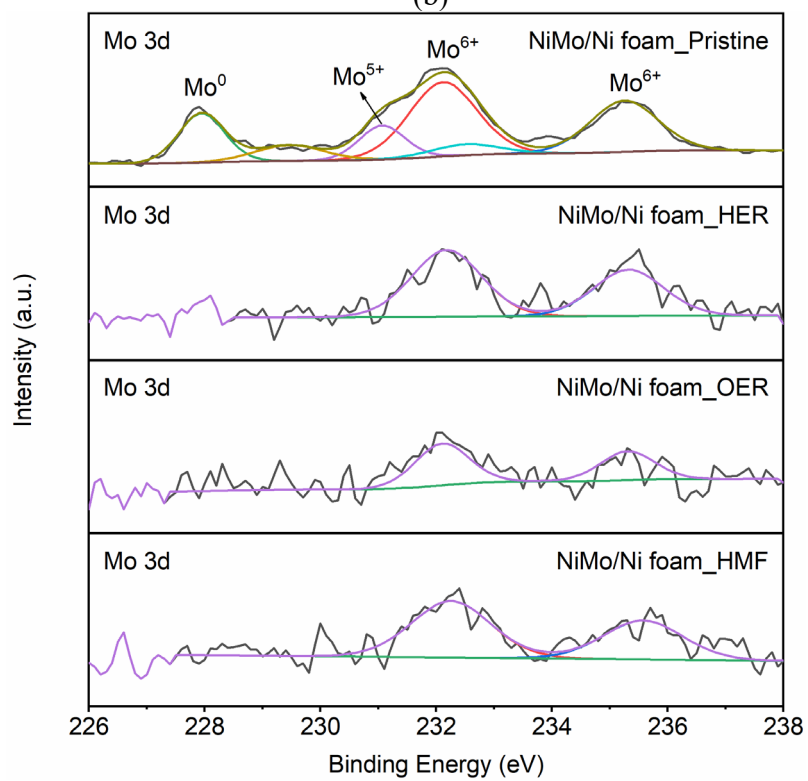
Figure S11. Raman spectra of the pristine NiMo/Ni foam electrode and the NiMo/Ni foam electrode after the HER, OER, and 5-HMF oxidation reaction.

As the NiMo catalyst is a metal alloy material, no signals can be obtained from the Raman spectra for the pristine sample, as shown in Figure S11. Following long-term HER, OER, and 5-HMF oxidation reaction, no obvious structural changes are apparent.





(b)



(c)

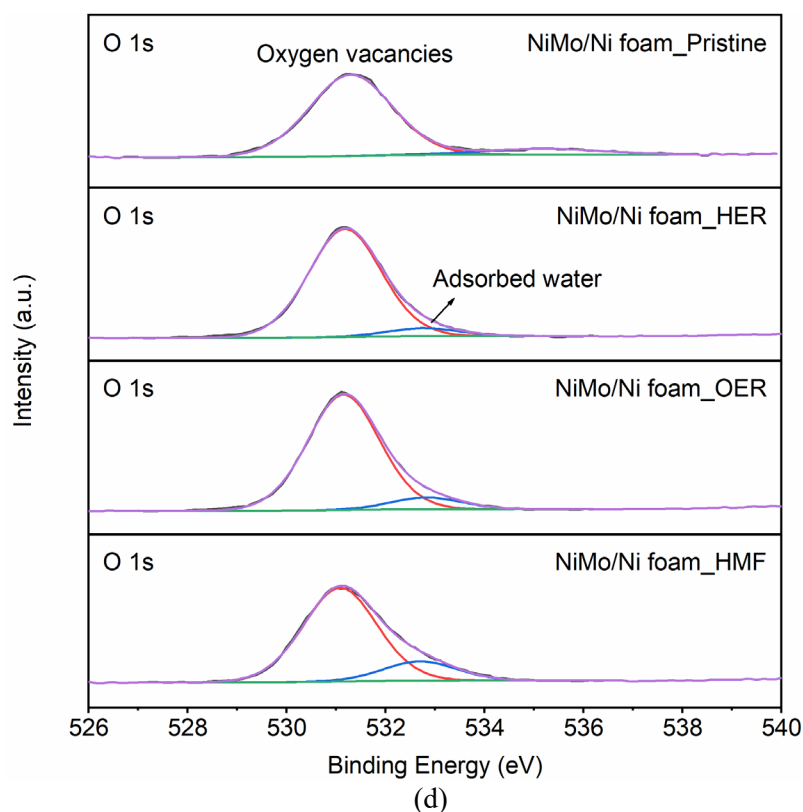


Figure S12. XPS spectra of the pristine NiMo/Ni foam and the NiMo/Ni foam electrode after the HER, OER, and 5-HMF oxidation reaction: (a) full survey, (b) Ni 2p, (c) O 1s, and (d) Mo 3d.

X-ray photoelectron spectroscopy (XPS) was performed to further explore the surface chemical composition and valence states of the pristine NiMo catalyst and those after long-term HER, OER, and 5-HMF oxidation reaction. The survey spectrum shows the presence of Ni, Mo, O, and C elements (Figure S12 a), where the O and C may arise from partial oxidation of the NiMo alloy on exposure to air and trace solvent residues. In the high-resolution Ni 2p_{3/2} spectrum (Figure S12 b), the peak located at 852.6 eV is attributed to the Ni⁰ valence state,²⁶ while the peak at 855.8 eV (in conjunction with its satellite peak at 861.2 eV) corresponds to the binding energies of Ni²⁺ due to the formation of nickel oxides on the surface.²³ After long-term operation for the HER, OER, or 5-HMF oxidation reaction, the surface Ni⁰ has been further oxidised to produce more nickel oxides/hydroxide, which is confirmed by the significantly smaller Ni⁰ peaks. The same phenomenon was observed for the valence state change to Mo in the various samples. As seen in the Mo 3d spectrum (Figure S12 c), Mo⁰ (227.8 eV), Mo⁵⁺ (231.1 eV), and Mo⁶⁺ (232.1 eV) co-exist in the pristine NiMo catalyst,²⁷ while the Mo⁰ and Mo⁵⁺ peaks disappear following the HER, OER, or 5-HMF oxidation reaction. In regards to the O 1s region (Figure S12 d), the peak at 531.3 eV in the pristine sample is indexed to oxygen vacancies in Ni/Mo oxides, with a growing peak at 532.8 eV representing the adsorbed water after the electrocatalytic activities. The XPS results demonstrate that the NiMo alloy undergoes structural reconstruction after the electrochemical reactions in alkaline solution.

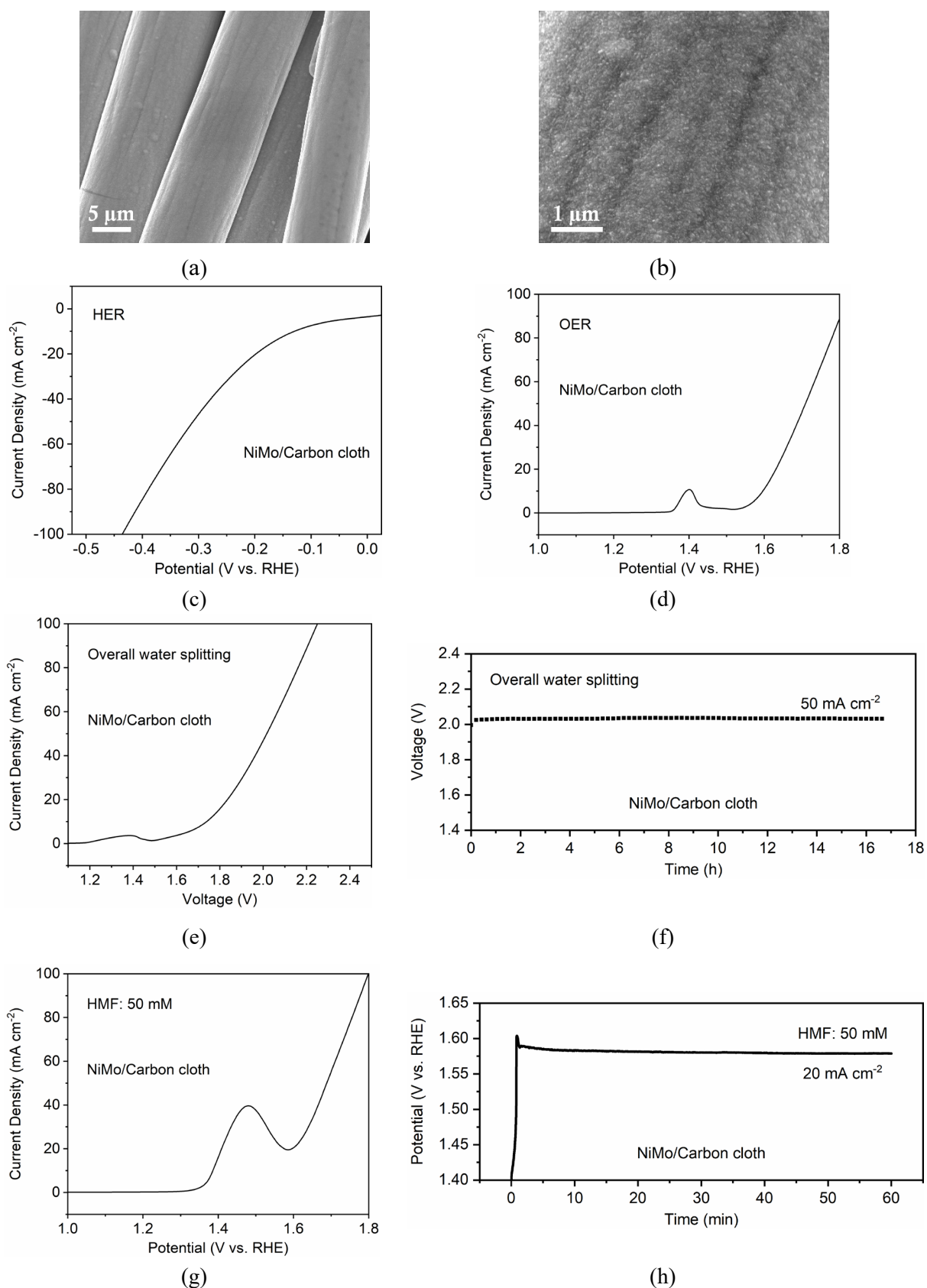


Figure S13. SEM images of NiMo alloy synthesized on carbon cloth at both (a) low and (b) high resolutions. LSV curves of the NiMo/carbon cloth electrode for (c) HER, (d) OER, and (e) overall water splitting. (f) Chronopotentiometry test of overall water splitting at 50 mA cm^{-2} for more than 16 hours. (g) LSV curve of the NiMo/carbon cloth electrode for 5-HMF oxidation reaction. (h) Chronopotentiometry test of 5-HMF oxidation at 20 mA cm^{-2} for 60 mins.

Compared with the NiMo alloy on Ni foam, the synthesized NiMo alloy/carbon cloth electrodes have similar morphology and good activity and durability towards the HER, OER, 5-HMF oxidation reaction, as well as overall water splitting. In Figure S13(h) for the 5-HMF oxidation durability test, the required potential (~ 1.58 V vs. RHE) at 20 mA cm^{-2} is higher than that (~ 1.41 V vs. RHE) obtained from the LSV curve in Figure S13 (g). This is because the chronopotentiometry test was conducted in a static electrolyte of a three-electrode cell, where the mass transfer of 5-HMF molecules becomes a major rate limiting step with time. In the studies utilising the flow electrolyser cell for 5-HMF conversion coupling hydrogen production, the circulating electrolyte alleviated the mass transfer issue.

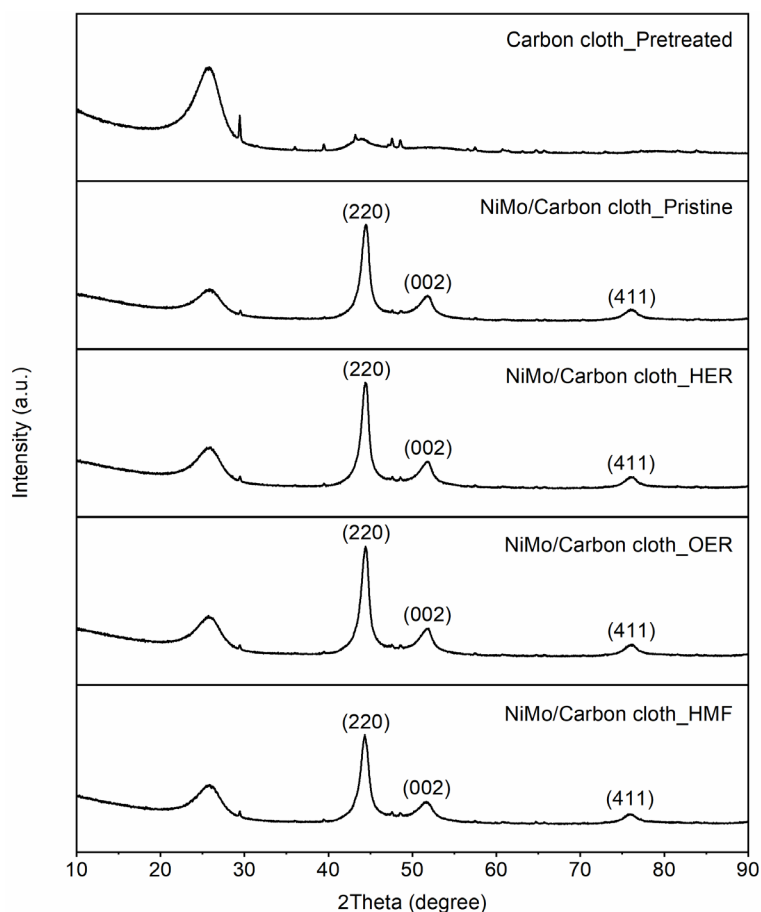


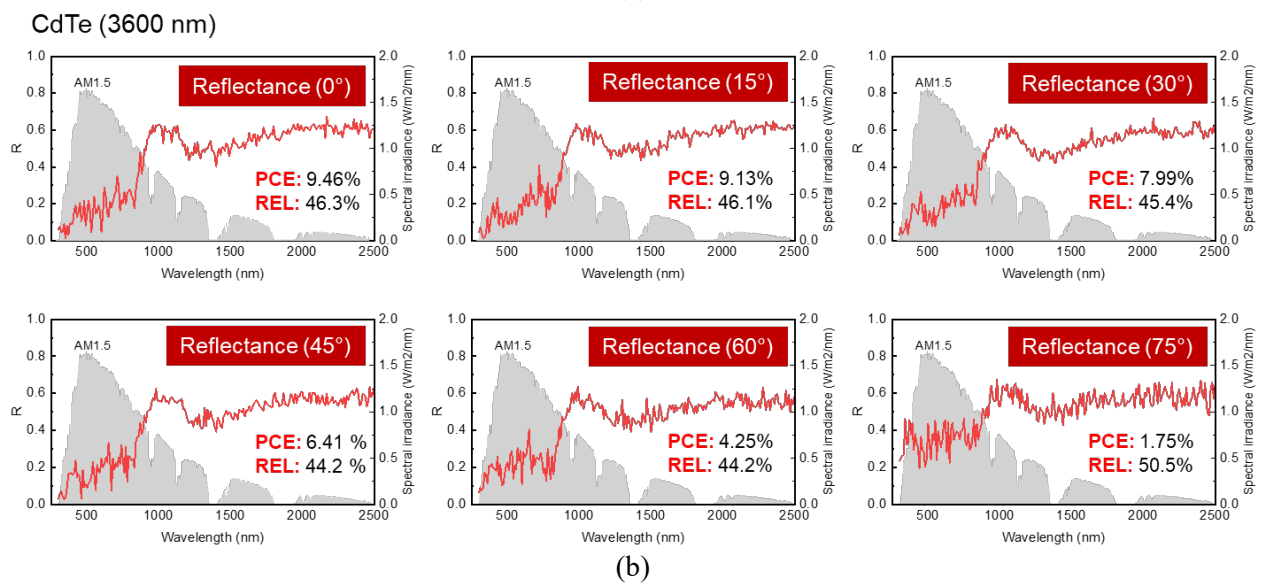
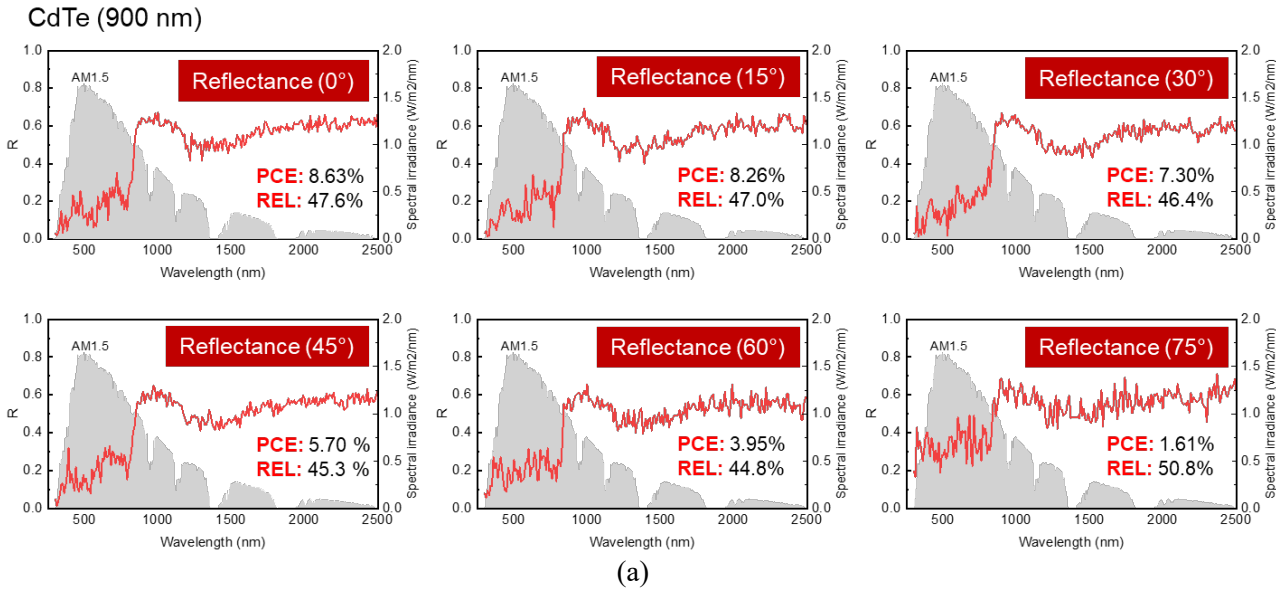
Figure S14. XRD patterns of pre-treated carbon cloth, as-synthesised NiMo/carbon cloth, and those after the HER, OER, and 5-HMF oxidation reaction.

The XRD patterns in Figure S14 exhibit the peaks of (220), (002), and (411) planes, which are indexed to a tetragonal structure (JCPDS #65-5480) of the Ni_4Mo phase.²⁸ Following the long-term HER, OER, 5-HMF oxidation reaction, the crystal structure does not change.

S3. Numerical modelling

Optical and electrical simulation: The potential of these concepts, including the design of solar cells and spectrum splitting applied in a hybrid PV-thermal configuration was investigated by optical and electrical modelling. An optical model was established using SunSolve™ software (PV Lighthouse Pty. Ltd., Australia), with the spectral response (absorption and reflectance) of the semi-reflectance CdTe solar cells with different CdTe absorber layer thicknesses (900, 1800 and 3600 nm) assessed. A second aspect to consider is how these cells will respond to light incident from angles other than standard normally-incident light.

Figure S15 (a-b) depicts the PV conversion efficiency (PCE), spectral reflectance and solar reflectance (REL) of the cell with different CdTe absorber thicknesses and at incident angles from 0 to 90 degrees, with the results summarized in Figure S15 (c). Additionally, Figure S15 (d) shows the optical reflectance results for the PV panel using a 520 nm diode laser module and a Thorlab photodetector, indicating good agreement between the simulation and experimental results.



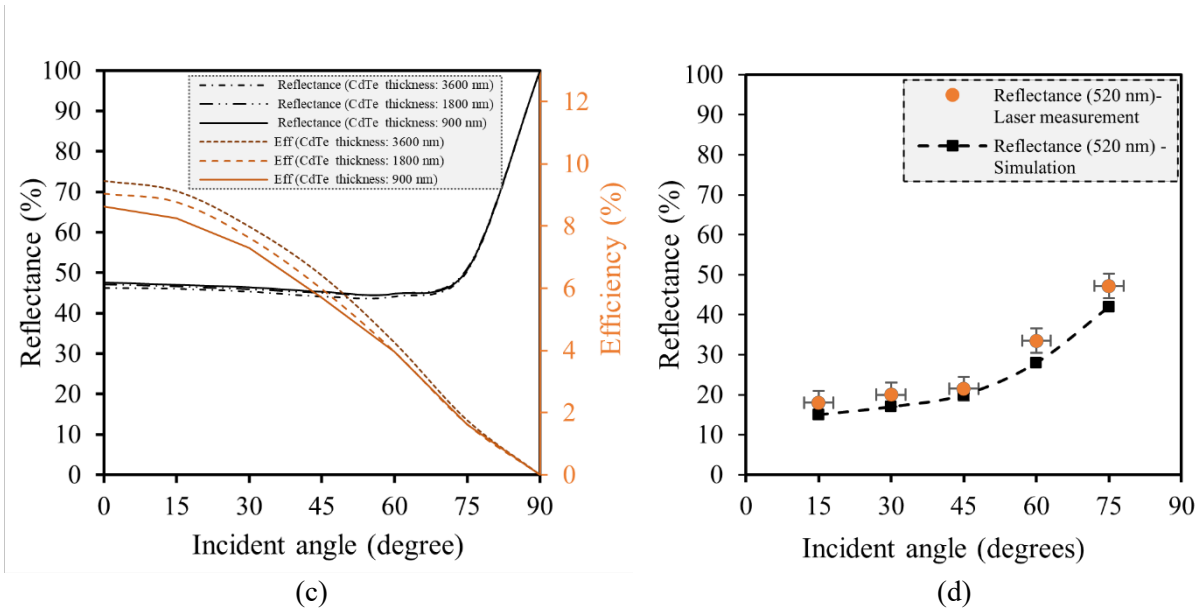


Figure S15. Performance of the CdTe cell: (a) reflectance and efficiency with 900 nm thickness CdTe layer at incident angle from 0 to 90 degrees; (b) reflectance and efficiency with 3600 nm thickness CdTe layer at incident angle from 0 to 90 degrees; (c) reflectance and efficiency at different incident angles with different CdTe absorber thickness; (d) reflectance of 520 nm wavelength light at 15 to 75 degrees.

Ray tracing simulations: Ray tracing simulation was conducted to assess the optical performance of the winged CPC (W-CPC) compared to a CPC using the COMSOL Multiphysics® software (“Geometrical optic” module). The realistic optical efficiency results of the CPC as a function of incident angles from 0° to 90° are shown in Figure S6, where the reflector’s spectral reflectance (0.90), transmittance of receiver’s outer glass tube (0.92) and receiver’s absorption (0.95) were considered.

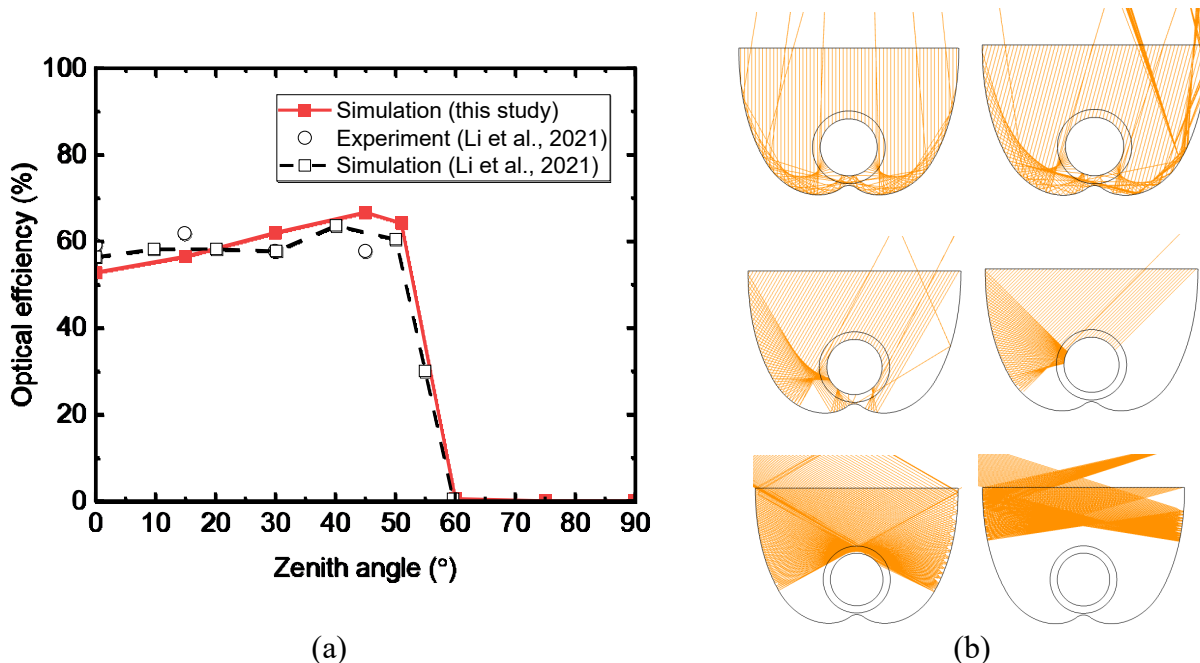


Figure S16. Performance of CPC with a half acceptance angle of 60°: (a) optical efficiency as a function of zenith/incident angle, compared with previous experimental work;¹⁰ (b) ray-trace analysis of the CPC for solar radiation incident angles $\theta = 0^\circ, \theta = 15^\circ, \theta = 30^\circ, \theta = 45^\circ, \theta = 60^\circ$ and $\theta = 75^\circ$.

S4. Additional experimental results

Solar optical/thermal efficiency measurement: The optical efficiency of a solar collector represents the portion of solar energy that reaches the absorber. It is the maximum practical efficiency of solar collectors. According to the solar thermal testing standard, EN 12975,²⁹ the optical efficiency can be assessed through its thermal efficiency of the solar collector operating close to ambient temperature (e.g. 20-40 °C) to minimize heat loss and can be defined by:³⁰

$$\eta_{optical} = \eta_{th} = \frac{M_f \times C_p \times \frac{dT_f}{dt}}{A_{BPR} \times G} \quad (S3)$$

where M_f and T_f are the mass and temperature of the operating fluid, respectively, G is the global solar irradiance in W/m^2 , C_p is the specific heat capacity of the fluid in $kJ/kg K$, A_{BPR} denotes the aperture area of the solar BPR and can be calculated based on the CPC aperture area:

$$A_{Aper_CPC} = W_{CPC} \times L_{CPC} \quad (S4)$$

where W_{CPC} and L_{CPC} are the width and length of the CPC. To account for off-normal incidence angles, the incidence angle modifier (IAM) can be determined using:²⁹

$$IAM = \frac{\eta_{opt}(\theta)}{\eta_{opt}(\theta = 0)} \quad (S5)$$

where $\eta_{opt}(\theta=0)$ is the optical efficiency at normal incidence. The IAM is usually measured in transversal and longitudinal components for collectors, $K_T(\theta_T)$ and $K_L(\theta_L)$. The IAM at an arbitrary incidence angle can be estimated by Eq. (S4). This approximation can lead to a small but acceptable error in the collected energy estimation.³¹

$$IAM = K(\theta) = K_T(\theta_T) \times K_L(\theta_L) \quad (S6)$$

According to solar thermal collector testing standard, EN 12975, the thermal efficiency can be determined by finding the coefficients of the following nonlinear equation.²⁹

$$\eta_{th} = a_0 - a_1 \frac{(T_m - T_a)}{G} - a_2 \frac{(T_m - T_a)^2}{G} \quad (S7)$$

where a_0 is the coefficient representing the optical efficiency (or highest thermal efficiency), which is affected by the incident angle modifier, reflectance of semi-reflective PV wing, the optical efficiency of the winged-CPC and the area ratio of PV cell to the whole collector:

$$a_0 = K(\theta) \times \rho_{PV} \times \eta_{o,W-CPC} \div \frac{A_{PV}}{A_{W-CPC}} \quad (S8)$$

where ρ_{PV} (see Figure 3(d) in the manuscript) is the solar reflectance of the PV wings. $\eta_{opt,W-CPC}$ denotes the optical efficiency of the winged-CPC, and the area ratio of the PV cell to the entire collector, A_{PV}/A_{W-CPC} , ranges from ~0.5 (only wings covered by PV cells, for the current work) to 1 (both wings and CPC have been covered by solar cells).

Solar thermal efficiency measurements were performed at a controlled incidence angle, for instance at normal incident angle ($\theta_T = 10^\circ$, $\theta_L = 0^\circ$), or at off-normal incidence angles (e.g., $\theta_T = 34^\circ$, $\theta_L = 0^\circ$; or $\theta_T = 0^\circ$, $\theta_L = 30^\circ$). The thermal efficiency can be calculated by testing various feed temperatures and solar radiation using Eq. (S3). By taking the thermal efficiency, η_{th} , as the dependent variable ‘Y’, and $x_1 = \frac{(T_m - T_a)}{G}$ and $x_2 = \frac{(T_m - T_a)^2}{G}$ as independent variables, the parameters a_0 , a_1 and a_2 can be identified using multiple linear regression. The experimental results revealed that the solar thermal

efficiency at normal incident angle ($\theta_T = 10^\circ$, $\theta_L = 0^\circ$ or at solar noon on summer solstice) can be expressed by:

$$\eta_{th} = 0.6 - 0.4 \frac{(T_f - T_a)}{G} - 0.005 \frac{(T_f - T_a)^2}{G} \quad (S9)$$

The solar thermal efficiency at an off-normal incident angle ($\theta_T = 34^\circ$, $\theta_L = 0^\circ$ or at solar noon on equinox) can be expressed by:

$$\eta_{th} = 0.62 - 0.4 \frac{(T_f - T_a)}{G} - 0.004 \frac{(T_f - T_a)^2}{G} \quad (S10)$$

with the coefficient results obtained from Eq. S9-S10, the value of $\eta_{o,W-CPC} = 0.6$, $a_1 = 0.4$, and $a_2 = 0.004$ are used to estimate any other off-normal incident angles. For instance, the solar thermal efficiency of the BPR at ($\theta_T = 15^\circ$, $\theta_L = 30^\circ$) can be estimated as:

$$\eta_{th} = 0.58 - 0.4 \frac{(T_f - T_a)}{G} - 0.004 \frac{(T_f - T_a)^2}{G} \quad (S11)$$

where the 0.58 was estimated by Eq.(S8), with $K(\theta) = 1.2$, $\rho_{PV} = 0.45$, $\eta_{opt,W-CPC} = 0.6$, and $A_{PV}/A_{W-CPC} = 0.5$.

In addition, if all surfaces of the solar collector (including flat wings and curved CPC components) are covered by semi-reflective PV cells, the efficiency of the PV winged BPR based on aperture area of CPC ($A_{aper,CPC}$) with an incident angle of θ can be expressed by:

$$\eta_{th} = 0.6 \cdot \rho_{pv} \cdot K(\theta) - 0.4 \frac{(T_f - T_a)}{G} - 0.004 \frac{(T_f - T_a)^2}{G} \quad (S12)$$

Water heating test: Figure S17 compares the temperature increase in a water-filled evacuated solar tube with and without the PV-CPC under the same operating conditions (incident angle: $\theta_T = 0-30^\circ$, $\theta_L = 30^\circ$; global solar radiation $G = 850 \pm 50 \text{ W/m}^2$, diffuse radiation: $G_d = 80 \pm 10 \text{ W/m}^2$, ambient temperature: $T_a = 20 \pm 3^\circ\text{C}$, tested on 6 May 2022 and 1 July 2022).

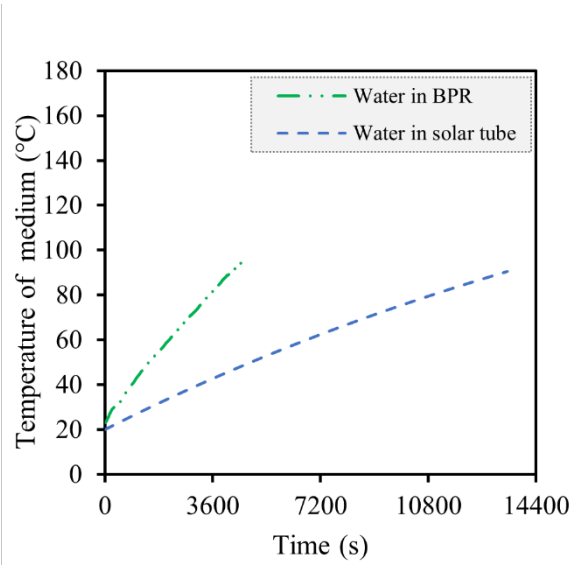


Figure S17. Water temperature increase in a water-filled evacuated solar tube with and without the PV-CPC

IV curve measurement of the CdTe panel: Three CdTe semi-transparent solar panels (purchased from Xiamen Solar First Energy Technology, China) were used for PV/T concept demonstration. The key characteristics are shown in Table S3.

Table S3. Key characteristics of the CdTe semi-transparent modules.

Parameters	Value (provided by supplier)	Value (measured under solar radiation of 900 W/m ²)
Size	550 x 280 x 7 mm	550 x 280 x 7mm
Maximum power at STC (P_{max})	10.8 (W)	11.0 W
Voltage at the maximum power point (V_{mp})	43.20 (V)	44.50 (V)
Current at the maximum power point (I_{mp})	0.25 (A)	0.244 (A)
Open circuit voltage (V_{oc})	58.10 (V)	56.81 (V)
Short circuit current (I_{sc})	0.29 (A)	0.30 (A)
Module efficiency	N/A	7.8 %
Fill factor	64%	64%
Transparency	50% (provided by supplier)	Measured results: 19% (405 nm); 34% (635 nm); 35% (520 nm);

The PCE of the solar panel can also be experimentally determined from current-voltage (I-V) characteristics under a standard illumination (AM1.5 solar simulator) or on-sun condition:

$$\eta_{el} = \frac{\max(I_{PV} \cdot V_{PV})}{P_{in}} \quad (S13)$$

where V_{PV} is the applied cell voltage and I_{PV} is the current in a solar cell.

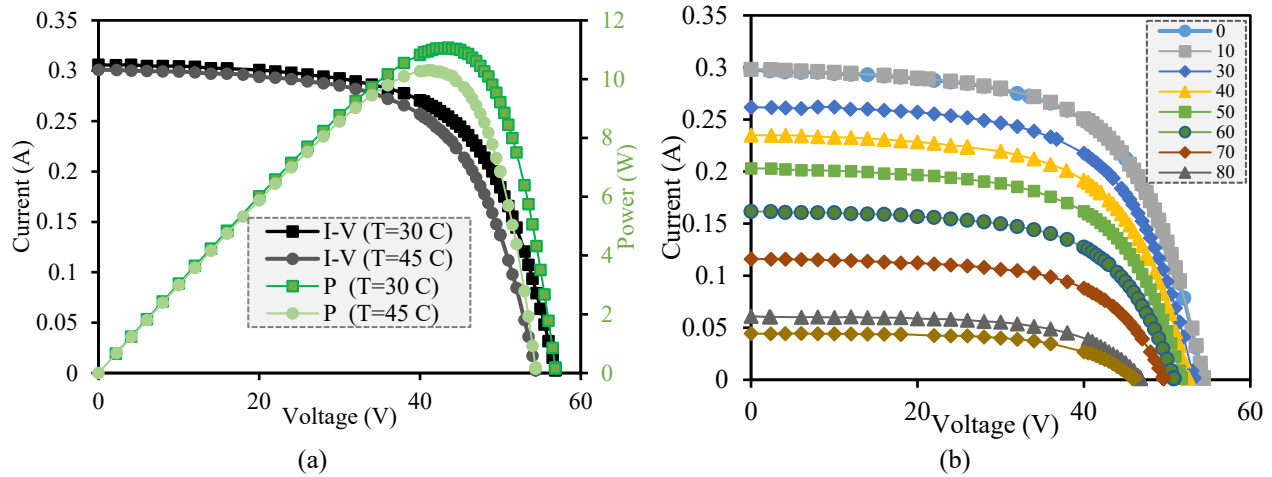


Figure S18. Performance of one CdTe panel/wing: (a) IV and output power curve of one CdTe panel at different surface temperatures; (b) efficiency of one CdTe panel at incident angle from 0 to 90 degrees (surface temperature was ~45 °C).

To improve solar to electrolysis power transfer efficiency, direct coupling between the PV system and the electrolyser can be realized by matching the current-voltage characteristics of the PVs with those of the electrolysers.^{32, 33} The general equation for the relationship between I-V of a PV cell is:

$$I = I_L - I_0 \left\{ \exp \left[\frac{q(V + IR_s)}{nkT} \right] - 1 \right\} - \frac{V + IR_s}{R_{sh}} \quad (S14)$$

where I is the PV cell output current [A], V the PV output voltage, I_L the photo generated current, I_0 is the dark saturation current, q the charge of electron [C], n the ideality factor (for thin film cells

it is 1), k is the Boltzmann's constant (1.38066×10^{-23} J/K), and T is the cell operating temperature [K]. R_s and R_{sh} are the series resistance and shunt resistance [Ω] at the module level.

If there are N number of cells in series connected in a module and M number of modules in parallel in an array, Eq. (S15) can be simplified by neglecting parallel resistance and series resistance.

$$I_{tot} = MI_L - MI_0 \left\{ \exp \left[\frac{q(V_{tot}/N + IR_s)}{nkT} \right] - 1 \right\} \quad (\text{S15})$$

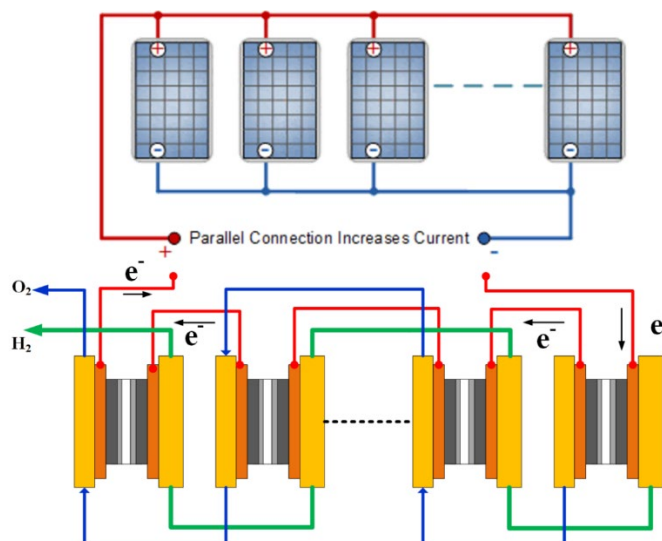


Figure S19. Direct coupling between the PV system and the electrolyser.

Hydrothermal treatment: A electrically heated hydrothermal Parr reactor system (series 4760 pressure vessel with volume of 450 mL and a Parr Model 4838 Reactor Controller, purchased from Parr Instrument, USA) was used to pre-condition the concentrated waste sugar solution in a sealed environment at a set temperature (e.g., 180 °C). While the indoor test conditions using the Parr reactor system (heating/cooling rate, maximum reaction temperature) can be controlled, on-sun tests experienced variations in received solar energy. An image of the Parr reactor system and a partial image of the solar thermal BPR are shown in Figure S20.

The temperature commonly used for biomass hydrothermal treatments lies between 120~250 °C, with a corresponding water saturation pressure of 2~40 bar. In this study, temperature of 120-180 °C were used (where the corresponding water saturation pressure varies from 2 to 10 bar). The range was selected as 120-180 °C (2 to 10 bar, 0.05 M sulfuric acid) is the recommended process conditions to maximize 5-HMF yield to ~22-25 mol % from 0.05-0.5 M sucrose.³⁴ A higher temperature can boost the reaction rate, but solar thermal collection efficiency decreases and other by-products (e.g., humins) form.³⁴ A second concern is the hazards associated with operating pressurised equipment (according to AS 4343:2014, Pressure equipment – Hazard levels). The solar thermal BPR design in this study comprised only an evacuated solar tube (borosilicate glass with an outer/inner tube diameter of 58/47mm and wall thickness of 1.6mm) which has a restricted tolerance to pressure (internal pressure limit is 10 bar as stated by the manufacturers including Apricus Australia Pty Ltd and Himin Solar).^{10, 35} A rupture of the seals/fittings or breakage of glass during the experiments could result in a release of the (hot and acidic) reaction fluid, which is a significant hazard. To minimise the hazard, the solar thermal BPR is currently being reconfigured to contain a C20 stainless-steel reaction vessel within the evacuated glass tube, which is more tolerant to high pressure (see Figure S20 c).

The BPR products were collected after each test (test 1-3 were performed using the solar thermal BPR, test 4 was performed using the Parr reactor). Precipitates/hydrochar were filtered with a 0.45 μm membrane before further analysis. The inset images in Figure 5(d) show the change in colour (from clear to yellowish-brown) of the product from the solar-thermal BPR for each test, illustrating the conversion of sugar to 5-HMF during the process. The yield of 5-HMF from sucrose conversion can be calculated by the following equation:

$$Y_{5\text{-HMF}} = \frac{\text{Moles of 5 - HMF produced}}{2 \cdot \text{Moles of sucrose initial}} = \frac{m_{5\text{-HMF}}/M_{5\text{-HMF}}}{2 \cdot m_{\text{sucrose}}/M_{\text{sucrose}}} \quad (\text{S16})$$

where M_{sucrose} (342.3 g/mol) and $M_{5\text{-HMF}}$ (126.11 g/mol) are the mole mass of the sucrose and 5-HMF, respectively, $m_{5\text{-HMF}}$ [g/L] is the mass of 5-HMF calculated from HPLC analysis, and m_{sucrose} is the initial mass of sucrose.

In addition, a dissolved organic carbon (DOC) content between 11,800 mg/L (from Test 4) and 12,600 mg/L (from Test 1) was detected in the BPR products, representing a 10~20% reduction in organic carbon from the feedstock (feedstock DOC ~ 13,000 mg/L) as precipitates/hydrochar separated from the product stream.

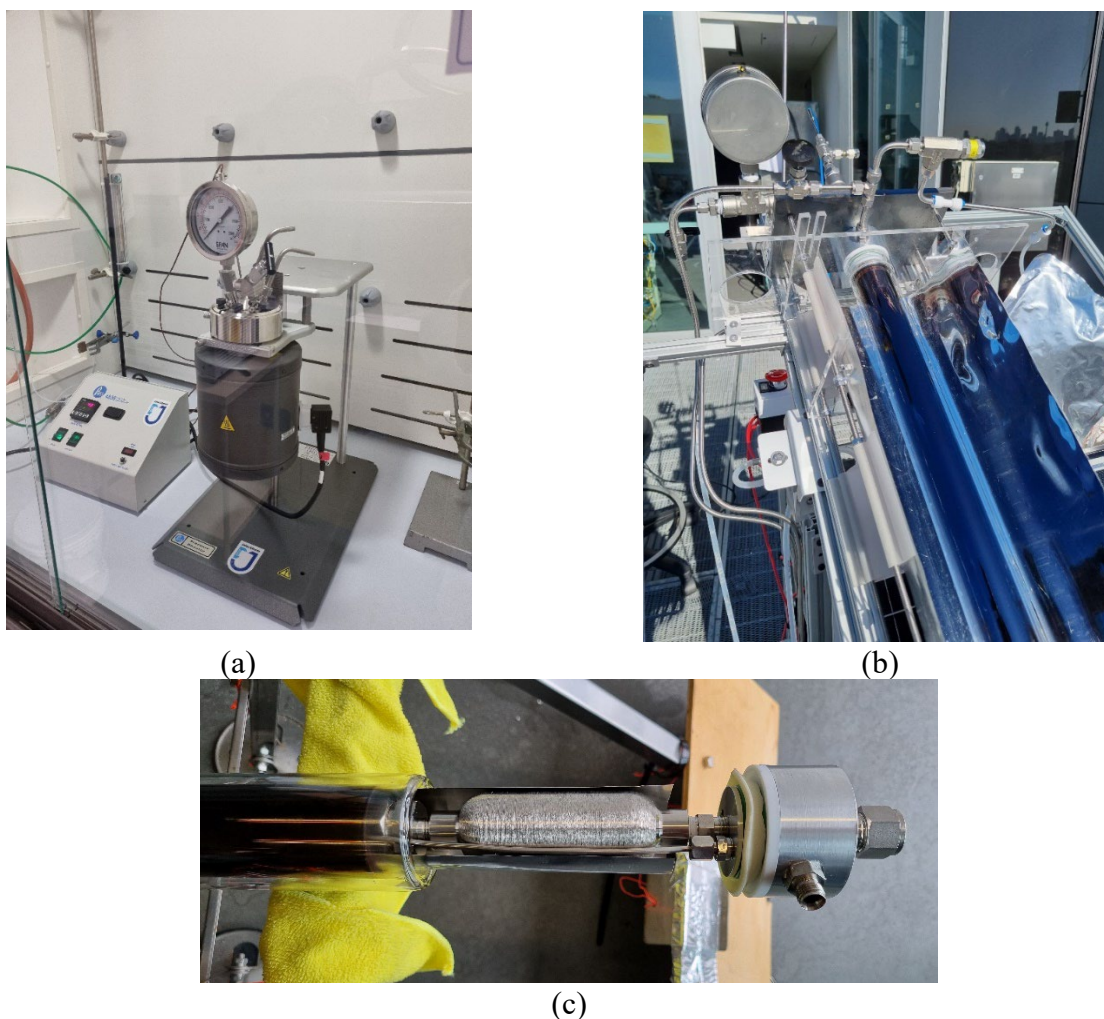


Figure S20. Hydrothermal reactors: (a) indoor Parr reactor system; (b) outdoor solar thermal BPR; (c) reconfigured BPR design.

Chromatographic analysis of 5-HMF and FDCA: Chromatographic analysis of 5-HMF and FDCA were conducted using a Shimadzu[®] LC-20-AD HPLC system interfaced with a photodiode array

detector. Separation of the analytes was performed on a Kinetex EVO column (5 μ m 150 mm x 4.6mm, Phenomenex, Australia). The HPLC was a 15-minute isocratic run and the mobile phase comprised water with 5 % of methanol and 0.1% of trifluoroacetic acid. The column oven was set at 60 °C. The flow rate and injection volume were 1 mL/min and 10 μ L, respectively. The diode array detector (DAD) recorded the spectra in the range from 200 to 400 nm, with detection of the analytes at specific wavelengths of 283 nm and 263 nm for quantification of 5-HMF and FDCA, respectively.

Stock standard solutions of 5-HMF and FDCA (obtained from Sigma Aldrich, Australia) were prepared in mobile phase (5 % of methanol and 0.1% of trifluoroacetic acid). The stock standard solutions were then diluted to a concentration range from 0 mM to 5 mM. Under the described analytical conditions, the 5-HMF peak eluted at 4.1 min with good retention time reproducibility while the FDCA peak appeared at 8.0 min, as shown in Figure S21 (c-d). From the corresponding peak areas obtained for the standard solutions, two calibration curves were generated over the range of 1-5 mM by identifying two linear relationships between peak area obtained from HPLC and 5-HMF concentration of the prepared standards. The calibration curves are illustrated in Figure S21 (a-b) with corresponding slope and intercept values.

After the calibration curves had been established, samples from the BPR or FEC were then prepared for HPLC testing. Roughly 10 mL was taken from the BPR and FEC product streams and placed into glass vials using a syringe with a 0.22 μ m PTFE filter. 10-time and 70-time dilutions were performed with the extracted samples in other HPLC autosampler vials (2 mL) to ensure clearly defined peak signals. Signal intensities obtained from the HPLC were used to calculate the 5-HMF and FDCA concentrations. After all tests were completed at each day, 65% (v/v) acetonitrile was used to clean the HPLC system and column. The chemicals used for the HPLC analysis are summarized in the Table S4.

Table S4. Materials/consumables for hydrolysis test and HPLC analysis.

Material items		Suppliers
	Sucrose (99 %)	
Standards for sucrose hydrothermal treatment	5-HMF (standards, \geq 99%)	Sigma Aldrich
	2,5-Furandicarboxylic acid (standards, 97%)	
HPLC- mobile phase (5 % methanol+ 0.1% of trifluoroacetic acid)	Methanol	Chem-supply® (Gillman, Australia)
	Trifluoroacetic acid (TFA)	
Column clean/store solution (acetonitrile 65%+Milli-Q 35%)	Acetonitrile (99.9%)	Chem-supply® (Gillman, Australia)
Filter	PTFE 0.22 μ m Syringe filter	BOJIN®

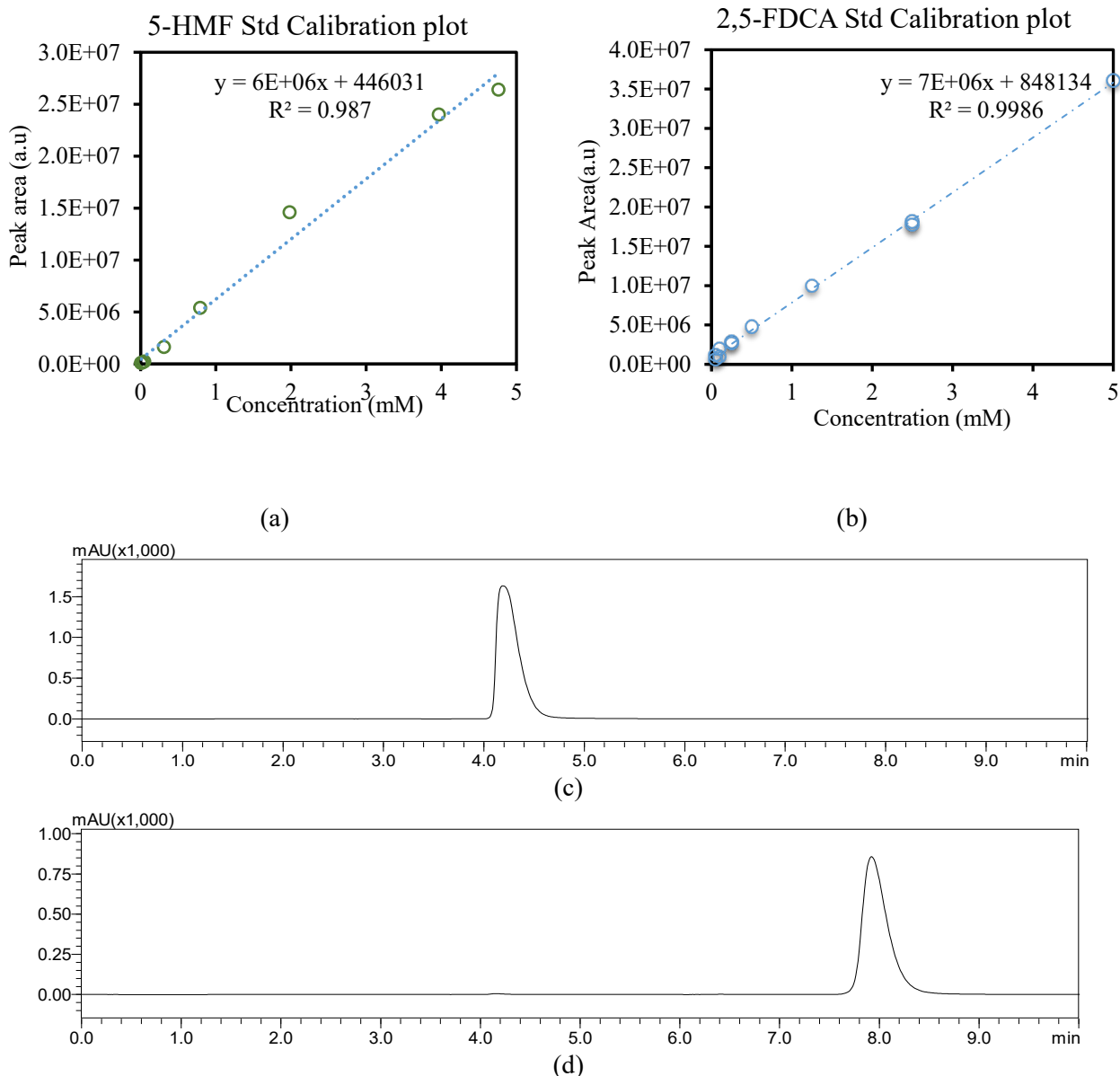


Figure S21. Chromatographic analysis of 5-HMF and FDCA: (a) 5-HMF standard calibration plot; (b) FDCA standard calibration plot; (c) chromatogram of a 5 mM 5-HMF standard solution; (d) chromatogram of a 1 mM FDCA standard solution.

Analysis of chemical oxygen demand (COD): Reduction of COD index is usually considered as a measure of the effectiveness of the wastewater treatment process. As reported in Table S1, the dichromate reflux method was used for COD determination. A calibration curve of light absorbance at 610 nm was prepared in the COD range from 0 to 15,000 mg/L for a standard COD solution, as shown in Figure S22(a). All the water samples were diluted 2 and 10 times prior to being tested. Figure S22(b) shows the COD of the concentrated sugar solution (35 g/L of sugar content) after hydrothermal treatment (test 3 using solar thermal BPR, conditions reported in Figure 5 of the manuscript) and electrooxidation (operated at 50 mA cm^{-2} for 12 hours, experimental conditions reported in Figure 6 of the manuscript). It was found that the COD of concentrated sugar solution decreased from $\sim 42 \text{ g/L}$ to 39 g/L after hydrothermal treatment using the BPR, and the COD of BPR product solution was reduced to 4 g/L after 12 hours of electrooxidation in the FEC. This may be explained by the hydrochar (biochar) formed during the BPR process, while organic matter degradation occurred during the FEC process. Thus, the results indicate that the hydrothermal treatment and electrooxidation processes can effectively

reduce COD. However, the current study focused on hydrogen production via biomass electrolysis. Separation/recovery of the target chemicals (e.g., 2,5-FDCA) and electrolyte management (e.g., electrolyte recycling, COD removal from waste electrolyte) will be investigated in future work.

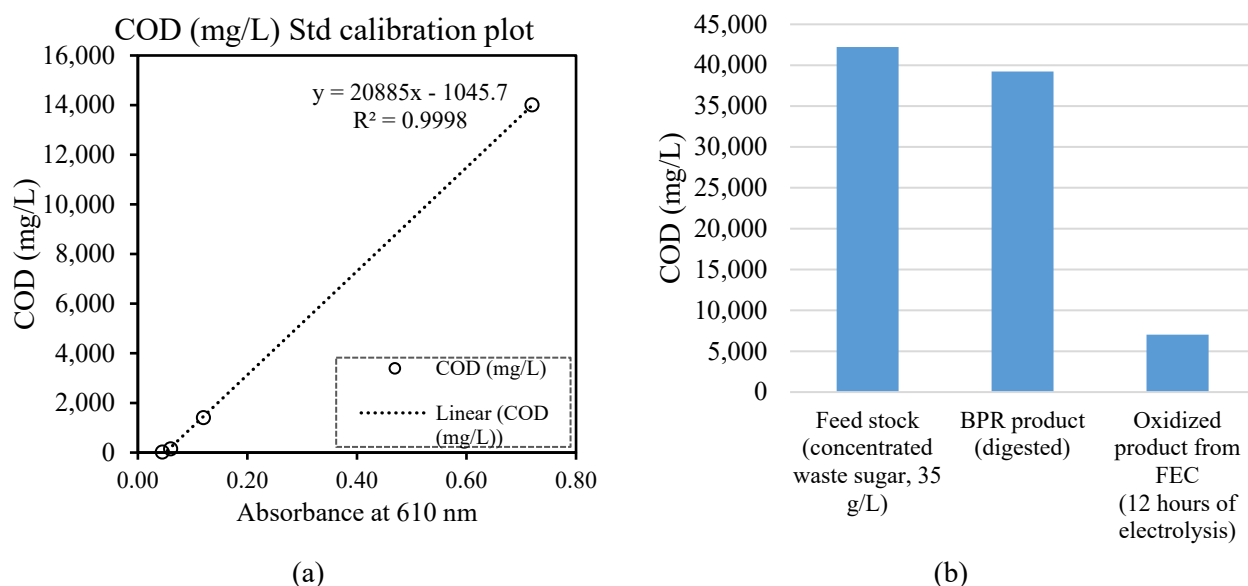


Figure S22. COD of the concentrated sugar solution after BPR preconditioning and FEC electrooxidation.

Solar-to-hydrogen (STH) conversion efficiency: The STH efficiency was calculated by multiplying the thermodynamic potential (V), the electrolysis current (I) and the Faradaic efficiency for hydrogen evolution (η_F), then dividing by the input solar power (P_{in}):

$$STH = \frac{P_{out}}{P_{in}} = \frac{V \cdot I \cdot \eta_F}{G \cdot A_{SC}} \quad (S17)$$

The Faradaic efficiency for hydrogen evolution (η_F), was calculated from total amount of hydrogen produced n_{H_2} (mol) and the total amount of electrons passed through the cell:

$$\eta_F = \frac{n_{H_2}}{Q/2F} = \frac{PV/RT [mol]}{I_E [A] \times t [S]/(2 \times 96485 [C/mol])} \quad (S18)$$

where P (101,325 pa) is the absolute pressure, V [m^3] is the measured hydrogen volume it produced per min, R is the gas constant ($8.3 \text{ J K}^{-1} \text{ mol}^{-1}$), and T is gas temperature (298 K). The total charge Q [C] was obtained from integration of the measured current I [A] over the time t [S] for 1 min, and F is the Faraday constant ($96,485 \text{ C mol}^{-1}$).

S5. Techno-economic assessment

The assumptions made for the techno-economic analysis in this work are provided in Table S5.

Table S5. Techno-economic analysis comparison considering two operating scenarios.

Parameters			Scenario 1	Scenario 2	References/ justifications
CAPEX (AU\$)	Biomass and electrolyte storage vessels	Total volume: 20 m ³	6,000	6,000	300 AU\$/m ³
	WBC (UF & RO based system)	Total membrane area 150 m ²	15,000	15,000	100 AU\$/m ² ³⁶
	PV-winged BPR	3 KW PV (50 m ² CdTe panel) + 18 KW (50 m ² CPC + 100 pcs solar tube reactor)	6,750	6,750	PV wing: 500 AU\$/kW; CPC: 100 AU\$/m ² ; solar tube reactor: 55 AU\$/piece. ^{10, 37}
	Additional PV system	10 kW	6,800	6,800	680 AU\$/kW ³⁸
	Electrolyser stacks	4 kW	3,000	3,000	750 AU\$/kW ³⁹
	Hydrogen storage vessel	33 kWh storage (1 kg H ₂)	5,000	5,000	
	Post-processing	Neutralizer reactor, and dryers	5,000	/	0.5 m ³ /day waste brine treatment
		Neutralizer reactor, crystallizers and dryers ⁴⁰	/	12,000	Resource (K ₂ SO ₄ , FDCA) recovery from 0.5 m ³ /day electrolyte ^{38, 41}
Others (instrumentation, piping, shipping, and installation)	/	14,000	14,000		
Total CAPEX (AU\$)			61,550	68,550	
OPEX (AU\$/year)	Consumables (e.g., chemicals)	~30 kg/day KOH (electrolyte), ~15 kg/day H ₂ SO ₄ (neutralization process)	12,000	12,000	KOH (1,220 AU\$/ton), H ₂ SO ₄ (213 AU\$/ton) ³⁸
	Maintenance	/	6,155	6,855	10% of % of initial CAPEX ³⁸
	OPEX (AU\$/year)		18,155	18,855	
Revenue stream	H ₂ production (kg/day)	1 kg /day	4 AU\$/day	4 AU\$/day	Hydrogen value: 4 AU\$/kg
	Clean water production (m ³ /day)	4.5 m ³ /day	10.5 AU\$/day	10.5 AU\$/day	Sydney water price: 2.35 AU\$/m ³
	Wastewater management	~60 kg of COD removed /day	60-120 AU\$/day	/	COD removal used in this study: 1-2 AU\$/kg COD _{removed} ⁴² (1-5 AU\$/kg COD _{removed} are reported in the literature ⁴³)
	FDCA production (kg/day)	1 kg /day	/	30-150 AU\$/day	Current market price of FDCA: 32-580 AU\$/kg ⁴⁴
	Total Revenue (AU\$/year), assuming 334 operation day/year		24,048-44,255 AU\$/year	20,875-54,275 AU\$/year	Sensitivity on waste management cost and the FDCA price is considered
Payback period (years)			3 - 14	1 - 20	

The payback period of the system (based on scaled-up system in Table 2 of main manuscript) was estimated by the capital expenses and cash flow generated per year. The cash flow was calculated by

inflow (yearly revenue, AU\$/year) and outflow of cash (operating expenses, AU\$/year). As indicated by Table S5, a 3-14 year payback period can be achieved in the first scenario which implements this system for organic wastewater treatment and hydrogen production (without the valuable by-product recovery). This result assumes a conservative estimate for the chemical oxygen demand (COD) removal cost of 1-2 AU\$/kg COD_{removed} (revenue of 60-120 AU\$/day), compared to 1-5 AU\$/kg COD_{removed} (revenue of 60-300 AU\$/day) as has been reported in the literature⁴³. Thus, implementing this system for organic wastewater treatment, clean water, and hydrogen production would be economically feasible (<5 years of payback period) if 82 AU\$/day of revenue can be generated from waste management. Implementation of this system for further valuable recovery (scenario 2) has a potential to further reduce the payback period. However, this payback time is highly dependent on the market price of FDCA (which can range from 32–580 AU\$/kg). Economic feasibility (<5 years of payback period) will be maintained if the market price of FDCA is higher than 90 AU\$/kg.

In any case, producing hydrogen alone would not be economically feasible for this system. It is only through the additional benefits/revenue from the production of (saleable) clean water, the offset cost of wastewater management, and the potential revenue from valuable by-products that enable the system to be economically feasible.

References

1. R. N. Comelli, L. G. Seluy, I. E. Grossmann and M. A. Isla, *Industrial & Engineering Chemistry Research*, 2015, **54**, 7687-7693.
2. M. Kasmi, A. Chatti, M. Hamdi and I. Trabelsi, *Clean Technologies and Environmental Policy*, 2016, **18**, 2265-2278.
3. A. Durán, J. M. Monteagudo, J. Gil, A. J. Expósito and I. San Martín, *Chemical Engineering Journal*, 2015, **270**, 612-620.
4. M. S. Sheldon and I. G. Erdogan, *Chemical Engineering Journal*, 2016, **285**, 368-377.
5. G. Peixoto, N. K. Saavedra, M. B. A. Varesche and M. Zaiat, *International Journal of Hydrogen Energy*, 2011, **36**, 8953-8966.
6. P. K. Poddar and O. Sahu, *Applied Water Science*, 2017, **7**, 461-468.
7. G. Güven, A. Perendeci and A. Tanyolac, *Chemical Engineering Journal*, 2009, **151**, 149-159.
8. D. A. Junior, C. E. Oro, M. S. dos Santos, R. M. Dallago and M. V. Tres, *Biointerface Res. Appl. Chem*, 2021, **11**, 12946-12957.
9. M. Castiglioni, L. Rivoira, M. Gallo, I. Ingrand, M. Del Bubba, B. Onida and M. C. Bruzzoniti, *Journal of Cleaner Production*, 2021, **324**, 129236.
10. Q. Li, Y. Zhuo, K. Shanks, R. A. Taylor, B. Conneely, A. Tan, Y. Shen and J. Scott, *Solar Energy*, 2021, **218**, 455-468.
11. L. Kranz, C. Gretener, J. Perrenoud, R. Schmitt, F. Pianezzi, F. La Mattina, P. Blösch, E. Cheah, A. Chirilă, C. M. Fella, H. Hagendorfer, T. Jäger, S. Nishiwaki, A. R. Uhl, S. Buecheler and A. N. Tiwari, *Nature Communications*, 2013, **4**, 2306.
12. M. Powalla, S. Paetel, E. Ahlswede, R. Wuerz, C. D. Wessendorf and T. M. Friedlmeier, *Applied Physics Reviews*, 2018, **5**, 041602.
13. M. M. Aliyu, M. A. Islam, N. R. Hamzah, M. R. Karim, M. A. Matin, K. Sopian and N. Amin, *International Journal of Photoenergy*, 2012, **2012**, 351381.
14. S. Ishizuka, Y. Kamikawa and J. Nishinaga, *npj Flexible Electronics*, 2022, **6**, 90.
15. M. I. Khalil, R. Bernasconi, A. Lucotti, A. Le Donne, R. A. Mereu, S. Binetti, J. L. Hart, M. L. Taheri, L. Nobili and L. Magagnin, *Journal of Applied Electrochemistry*, 2021, **51**, 209-218.
16. W. Dai, Z. Gao, J. Li, S. Qin, R. Wang, H. Xu, X. Wang, C. Gao, X. Teng, Y. Zhang, X. Hao, Y. Wang and W. Yu, *ACS Applied Materials & Interfaces*, 2021, **13**, 49414-49422.
17. W. Dai, Z. Gao, J. Li, S. Qin, R. Wang, H. Xu, X. Wang, C. Gao, X. Teng, Y. Zhang, X. Hao, Y. Wang and W. Yu, *ACS Applied Materials & Interfaces*, 2021, DOI: 10.1021/acsami.1c11493.
18. J. Ramanujam and U. P. Singh, *Energy & Environmental Science*, 2017, **10**, 1306-1319.

19. M. Stanley, M. Jubault, F. Donsanti and N. Naghavi, *physica status solidi c*, 2017, **14**, 1700174.
20. X. Li, P. Li, Z. Wu, D. Luo, H.-Y. Yu and Z.-H. Lu, *Materials Reports: Energy*, 2021, **1**, 100001.
21. M. Stanley, M. Jubault, S. Gaiaschi, A. Tempez, F. Donsanti and N. Naghavi, *Thin Solid Films*, 2019, **671**, 6-11.
22. W. Hsu, C. M. Sutter-Fella, M. Hettick, L. Cheng, S. Chan, Y. Chen, Y. Zeng, M. Zheng, H.-P. Wang, C.-C. Chiang and A. Javey, *Scientific Reports*, 2015, **5**, 16028.
23. M. Y. Gao, C. Yang, Q. B. Zhang, J. R. Zeng, X. T. Li, Y. X. Hua, C. Y. Xu and P. Dong, *Journal of Materials Chemistry A*, 2017, **5**, 5797-5805.
24. K. Kordek, L. Jiang, K. Fan, Z. Zhu, L. Xu, M. Al - Mamun, Y. Dou, S. Chen, P. Liu, H. Yin, P. Rutkowski and H. Zhao, *Advanced Energy Materials*, 2018, **9**.
25. Y. Bai, Y. Wu, X. Zhou, Y. Ye, K. Nie, J. Wang, M. Xie, Z. Zhang, Z. Liu, T. Cheng and C. Gao, *Nat Commun*, 2022, **13**, 6094.
26. A. P. Grosvenor, M. C. Biesinger, R. S. C. Smart and N. S. McIntyre, *Surface Science*, 2006, **600**, 1771-1779.
27. Z. Wang, J. Chen, E. Song, N. Wang, J. Dong, X. Zhang, P. M. Ajayan, W. Yao, C. Wang, J. Liu, J. Shen and M. Ye, *Nat Commun*, 2021, **12**, 5960.
28. Y. Wang, G. Zhang, W. Xu, P. Wan, Z. Lu, Y. Li and X. Sun, *ChemElectroChem*, 2014, **1**, 1138-1144.
29. P. Kovacs, *Technical Research Institute of*, 2012.
30. A. Hassanzadeh, L. Jiang and R. Winston, *Solar Energy*, 2018, **173**, 1248-1261.
31. T. Osório, P. Horta and M. Collares-Pereira, *Renewable Energy*, 2019, **133**, 1086-1098.
32. B. Paul and J. Andrews, *International Journal of Hydrogen Energy*, 2008, **33**, 490-498.
33. N. A. Burton, R. V. Padilla, A. Rose and H. Habibullah, *Renewable and Sustainable Energy Reviews*, 2021, **135**, 110255.
34. J. N. M. Tan-Soetedjo, H. H. van de Bovenkamp, R. M. Abdilla, C. B. Rasrendra, J. van Ginkel and H. J. Heeres, *Industrial & Engineering Chemistry Research*, 2017, **56**, 13228-13239.
35. Specification of all glass evacuated tube, <http://himinsun.com/2-1-glass-evacuated-tube.html>, 2023).
36. Q. Li, B. Lian, Y. Wang, R. A. Taylor, M. Dong, T. Lloyd, X. Liu, J. Tan, M. M. Ashraf, D. Waghela and G. Leslie, *Water Research*, 2018, **144**, 642-655.
37. B. Widylar, L. Jiang, J. Ferry and R. Winston, *Applied Energy*, 2018, **216**, 521-533.
38. M. A. Khan, T. A. Al-Attas, N. G. Yasri, H. Zhao, S. Larter, J. Hu and M. G. Kibria, *Sustainable Energy & Fuels*, 2020, **4**, 5568-5577.
39. J. Yates, R. Daiyan, R. Patterson, R. Egan, R. Amal, A. Ho-Baille and N. L. Chang, *Cell Reports Physical Science*, 2020, **1**, 100209.
40. R. Latsuzbaia, R. Bisselink, A. Anastasopol, H. van der Meer, R. van Heck, M. S. Yagüe, M. Zijlstra, M. Roelands, M. Crockatt, E. Goetheer and E. Giling, *Journal of Applied Electrochemistry*, 2018, **48**, 611-626.
41. J. H. Kim, J.-G. Na, J.-W. Yang and Y. K. Chang, *Bioresource Technology*, 2013, **140**, 64-72.
42. I. Sanni, M. R. Karimi Estahbanati, A. Carabin and P. Drogui, *Separation and Purification Technology*, 2022, **282**, 119992.
43. S. Metin and D. İ. Çifçi, *Journal of Chemical Technology & Biotechnology*, 2023, **98**, 1158-1165.
44. J. Na, B. Seo, J. Kim, C. W. Lee, H. Lee, Y. J. Hwang, B. K. Min, D. K. Lee, H.-S. Oh and U. Lee, *Nature Communications*, 2019, **10**, 5193.